Peer-reviewed version available at *Remote Sensing* **2020**, *12*; doi:10.3390/rs12152430

Article

LiCSAR: An Automatic InSAR Tool for Measuring and Monitoring Tectonic and Volcanic Activity

Milan Lazecký [1], Karsten Spaans [2], Pablo J. González [3,4], Yasser Maghsoudi [1], Yu Morishita [1,5], Fabien Albino [6], John Elliott [1], Nicholas Greenall [7], Emma Hatton [1], Andrew Hooper [1], Daniel Juncu [1], Alistair McDougall [8], Richard J. Walters [9], C. Scott Watson [1], Jonathan R. Weiss [1,10], and Tim J. Wright [1].

[1] COMET, School of Earth and Environment, University of Leeds, Leeds LS2 9JT, UK; M.Lazecky@leeds.ac.uk (M.L.); Y.Maghsoudi@leeds.ac.uk (Y.M.); morishita-y96pt@mlit.go.jp (YuM.); J.Elliott@leeds.ac.uk (J.E.); emma.hatton@protonmail.com (E.H.); A.Hooper@leeds.ac.uk (A.H.); D.Juncu@leeds.ac.uk (D.J.); c.s.watson@leeds.ac.uk (C.S.W); jonathan.weiss@uni-potsdam.de (J.R.W.); T.J.Wright@leeds.ac.uk (T.J.W.);

[2] SatSense Ltd., Leeds Innovation Centre, 103 Clarendon Road, Leeds LS2 9DF, UK; karsten.spaans@satsense.com

[3] COMET, Department of Earth, Ocean and Ecological Sciences, University of Liverpool, Liverpool L69 3BX, UK; pablo.jose.gonzalez-mendez@liverpool.ac.uk (P.G.)

[4] Volcanology Research Group, Department of Life and Earth Sciences, IPNA-CSIC, Tenerife, Spain

[5] Geography and Crustal Dynamics Research Center, Geospatial Information Authority of Japan, Tsukuba 305-0811, Japan

[6] COMET, School of Earth Sciences, University of Bristol, Senate House, Tyndall Ave, Bristol BS8 1TH, UK; fa17101@bristol.ac.uk (F.A.)

[7] Independent software developer; lnrg.nick@gmail.com (N.G.)

[8] Independent researcher; alistair.mcdougall@gmail.com (A.M.)

[9] COMET, Department of Earth Sciences, Durham University, Durham UK; richard.walters@durham.ac.uk

[10] Institute of Geosciences, University of Potsdam, Potsdam, Germany

- Correspondence: M.Lazecky@leeds.ac.uk (M.L.)

Abstract:

Space-borne Synthetic Aperture Radar (SAR) Interferometry (InSAR) is now a key geophysical tool for surface deformation studies. The European Commission's Sentinel-1 Constellation began acquiring data systematically in late 2014. The data, which are free and open access, have global coverage at moderate resolution with a 6 or 12-day revisit, enabling researchers to investigate large-scale surface deformation systematically through time. However, full exploitation of the potential of Sentinel-1 requires specific processing approaches as well as the efficient use of modern computing and data storage facilities. Here we present LiCSAR, an operational system built for large-scale interferometric processing of Sentinel-1 data. LiCSAR is designed to automatically produce geocoded wrapped and unwrapped interferograms and coherence estimates, for large regions, at 0.001° resolution (WGS-84 system). The products are continuously updated in a frequency depending on prioritised regions (monthly, weekly or live update strategy). The products are open and freely

Peer-reviewed version available at *Remote Sensing* **2020**, *12*; doi:10.3390/rs12152430

accessible and downloadable through an online portal. We describe the algorithms, processing, and storage solutions implemented in LiCSAR, and show several case studies that use LiCSAR products to measure tectonic and volcanic deformation. We aim to accelerate the uptake of InSAR data by researchers as well as non-expert users by mass producing interferograms and derived products.

Keywords: SAR Interferometry; Sentinel-1; deformation monitoring; tectonics; volcanism; automatic processing;

1. Introduction

With the advent of the European Commission's Copernicus two-satellite Sentinel-1 constellation, operated by the European Space Agency (ESA), a massive volume of high-quality C-band Synthetic Aperture Radar (SAR) observations with moderate spatial (2-14m) and temporal resolution (6-12 days) has become freely available [1]. With a 250-km-wide cross-track coverage in the default Interferometric Wide Swath (IWS) mode, Sentinel-1 provides a unique and powerful dataset that has the potential to be used for monitoring surface deformation at spatial scales ranging from a few meters to tens of kilometers. Interferometric Synthetic Aperture Radar (InSAR) is a particularly suitable technique for measuring deformation induced by various geophysical phenomena, including the coseismic [2-4], postseismic [5-8] and interseismic phases of the earthquake deformation cycle [9-12], volcanic movements [13-15], terrain deformation due to geothermal activities [16-18] and slow-moving landslides [19,20]. Since the launch of Sentinel-1B in 2016, data are acquired globally with a typical revisit period of 12 days, and every 6 days in Europe [21]. The relatively short revisit time (compared to 35-days of previous ESA SAR satellites) is a significant advance because interferograms spanning a short interval usually maintain better coherence and allow a more accurate estimate of rapid deformation. The short revisit time also leads to a greater number of acquisitions, which is useful for statistical reduction of the noise contribution (e.g. due to atmospheric phase delay) in InSAR time series analyses [22]. The data is particularly important for global monitoring of tectonic and volcanic activities [23]. Over the last five years, numerous earthquakes and volcanic eruptions have already been imaged by Sentinel-1 interferograms, aiding rapid response and resulting in a greater scientific understanding of the events and their geophysical properties [8,24-26].

Despite the opportunities provided by the increasing availability of Sentinel-1 SAR data, it is still difficult to take full advantage of these resources particularly for large-scale applications. Indeed, the full exploitation of the large amount of SAR data provided by the Sentinel-1 system, with its short revisit time and global-scale coverage (data are produced in the rate of ~13 TB/day), requires specific data preprocessing approaches (e.g. downsampling the SAR data – multilooking) or Big Data processing algorithms involving computer cluster facilities. The computing and storage demands require specific computing platforms [27]. Various research groups base their systematic processing approaches on open-source software such as SNAP [28], ISCE [29] or GMTSAR [30] for generation of differential interferograms and GMTSAR, STAMPS [31] or other tools as their time series processor. Other institutions prefer commercial software equivalents such as GAMMA [32,33], ENVI SARScape [34] or SARPROZ [35], to list the currently most recognized available tools. As the deployment of an InSAR processing system is strongly connected to the storage and computing facilities required, there is currently a lack of recognized deployable system solutions, although with exceptions such as IT4S1 [36], which is partly based on the metadata database approach described in this work.

In recent years, there has been remarkable developments in promoting the idea of using cloud computing technology to address the storage and processing of remote sensing data. Significant efforts are underway to facilitate access to high-performance computing (HPC) resources and processing of very large Earth Observation (EO) datasets by such institutions as the National Aeronautics and Space Administration (NASA), the United States Geological Survey (USGS),

Peer-reviewed version available at Remote Sensing 2020, 12; doi:10.3390/rs12152430

company-based infrastructures such as the Google Earth Engine (GEE), the Amazon Web Services (AWS), or science oriented HPC platforms such as the Earth Observation Data Center (EODC) [37]. In 2018, the European Commission publicly launched the Copernicus Data and Information Access Services (DIAS). These cloud-based systems not only allow access to EO datasets but also provide processing resources and tools for data analytics and allow for a scalable computing environment [38]. Similarly, NASA's Alaska Satellite Facility (ASF) has provided a platform for archiving and distributing Sentinel-1 data at ASF Distributed Active Archive Centers (DAAC). Besides the Sentinel-1 data, ASF DAAC is storing data from a variety of different SAR sensors, including both historic and modern missions. The data are distributed using Vertex, ASF's data search website, as well as ASF's Application Programming Interface (API). These platforms have reduced technological barriers for conducting large-area mapping and thus may stimulate a surge of global or regional maps. With these platforms, it is much easier to process these data remotely in the cloud without downloading large datasets to a local computer. However, they are mainly focused on the provision of data with some preliminary processing tools and are not designed to mass produce products for non-specialist users and make them openly accessible.

Besides the above-mentioned platforms, ESA has developed "EO Exploitation Platforms (EPs)" that represent a set of research and development activities aimed at the creation of an ecosystem of interconnected "Thematic Exploitation Platforms (TEPs)". TEPs are collaborative, virtual work environments providing access to EO data and the tools, processors, and IT resources required using one coherent interface. The TEPs have been implemented to address the most important topics in remote sensing i.e. Coastal, Forestry, Hydrology, Geohazards, Polar, Urban, and Food Security [39]. For the context of this paper concerning applications to tectonics, earthquakes and volcanoes, it suffices to introduce the Geohazard Exploitation Platform (GEP). GEP is ESA's web-based platform that is specially designed to exploit EO data for assessing geohazards associated with active seismicity, volcanism, subsidence, or landslides [40]. GEP serves as a user-friendly interface to run various web tools implemented in the ESA's Grid Processing on Demand (G-POD) environment [41]. Some of these web tools can be used for generation of differential interferograms (e. g. DIAPASON) or for multi-temporal InSAR processing, especially based on implementation of Small Baselines (SB) algorithms [42]. GEP is based on a collaborative work environment for the development, integration and exploitation of different services [43]. It mainly provides on-demand processing services for specific user needs and the InSAR tools do not provide interferometric products at a global scale.

With slightly different aims, NASA JPL has developed an Advanced Rapid Imaging and Analysis (ARIA) system, which automatically generates SAR-derived data products, primarily from the Sentinel-1 mission. It incorporates an automatic processing chain to generate co-seismic interferograms in response to major earthquakes and recently it has begun to provide standard InSAR displacement products, allowing users to circumvent the use of specialized radar processing software altogether and make InSAR products more accessible for science applications [44]. However, ARIA also does not currently plan to mass produce products over large regions for long time series analysis.

Here, we present activities carried out for the design, development, integration, and deployment of a fully automated state-of-the-art InSAR processing chain for Sentinel-1 data developed within the Looking Inside the Continents from Space (LiCS) project by COMET, the Centre for the Observation and Modelling of Earthquakes, Volcanoes and Tectonics. The LiCS project primarily aims at understanding how the continents deform at all spatial and temporal scales, with a focus on using observations of the earthquake deformation cycle to understand how seismic hazard is distributed in space and time. For this purpose, an automated InSAR processing system, LiCSAR, has been developed. LiCSAR is capable of processing Sentinel-1 data acquired globally, with the resulting products freely accessible and downloadable through an online portal, including both wrapped and unwrapped interferograms, coherence estimates, time series and other products. Innovative algorithmic, processing and storage solutions have been implemented to allow us to reduce the computing time and the required disk space.

This article is organised as follows. Section 2 presents the architecture and the main features of the LiCSAR processing system, providing basic information about facilities, data and metadata storage system and processing chain strategies, including description of the current earthquake responder. Section 3 describes LiCSAR interferometric data products, their formats, structure and their update strategy. In Section 4, we will review how various tectonic, earthquake and volcanic applications benefit from the LiCSAR system, and illustrate this using recent results obtained in the Alpine-Himalayan belt. Finally, the conclusions and plans for further developments of the system are given in the Section 5.

2. LiCSAR System Architecture

The LiCSAR system consists of several interconnected modules. The LiCSAR processing chain, described in Section 2.1, uses various custom tools and algorithms over the core processing functionality that is based on advanced commercial software for processing SAR data, GAMMA [45]. LiCSAR processing is performed over systematic geographical spatial extents termed frames. A frame is defined as a collection of Sentinel-1 IWS burst units imaged during the satellite's pass within a given orbital track. We have created custom LiCSAR burst unit identifiers. Metadata for each of these burst units are extracted from Sentinel-1 Single Look Complex (SLC) acquisitions and registered in the LiCSInfo metadata database that handles burst and frame definitions (see Section 2.2).

We extract and merge bursts covering a frame into SLC mosaics for each acquisition epoch. Afterwards we coregister and resample these SLC mosaics to the geometry of a primary SLC acquisition, which is set during the initialisation of the frame. We then use the resampled SLC (RSLC) data to form interferometric products (wrapped and unwrapped interferograms, and coherence maps) by combining the new RSLC with, by default, four chronologically preceding ones, and georeference them to WGS-84 coordinate system. The whole process is automated and optimised for effective batch processing in computer clusters, and identified as LiCSAR FrameBatch toolbox, described in Section 2.3. LiCSAR FrameBatch is a standard tool used for updating frame datasets and is called by other specific tools, such as LiCSAR Earthquake Responder, described in Section 2.4.

We show a general overview of the LiCSAR system architecture in a flowchart in Figure 1. The whole system is closely aligned to the technical infrastructure offered by the Centre for Environmental Data Analysis (CEDA), see Section 2.5. Here, both data storage (CEDA Archive, internal and public LiCSAR data storages) and computing facilities are synchronised with the metadata database (LiCSInfo, see Section 2.2) and LiCSAR processing chain to prepare InSAR outputs. The flowchart in Fig. 1 also shows a connection to the COMET Generic Atmospheric Correction Online Service (GACOS) system [46], allowing for routine corrections of tropospheric delay in interferograms using atmospheric weather models. The procedure to acquire GACOS data has been not fully automated yet, as the current API requests for generating GACOS data would prolong the LiCSAR products generation process. GACOS data per frame are currently being generated upon request.

Peer-reviewed version available at *Remote Sensing* **2020**, *12*; doi:10.3390/rs12152430

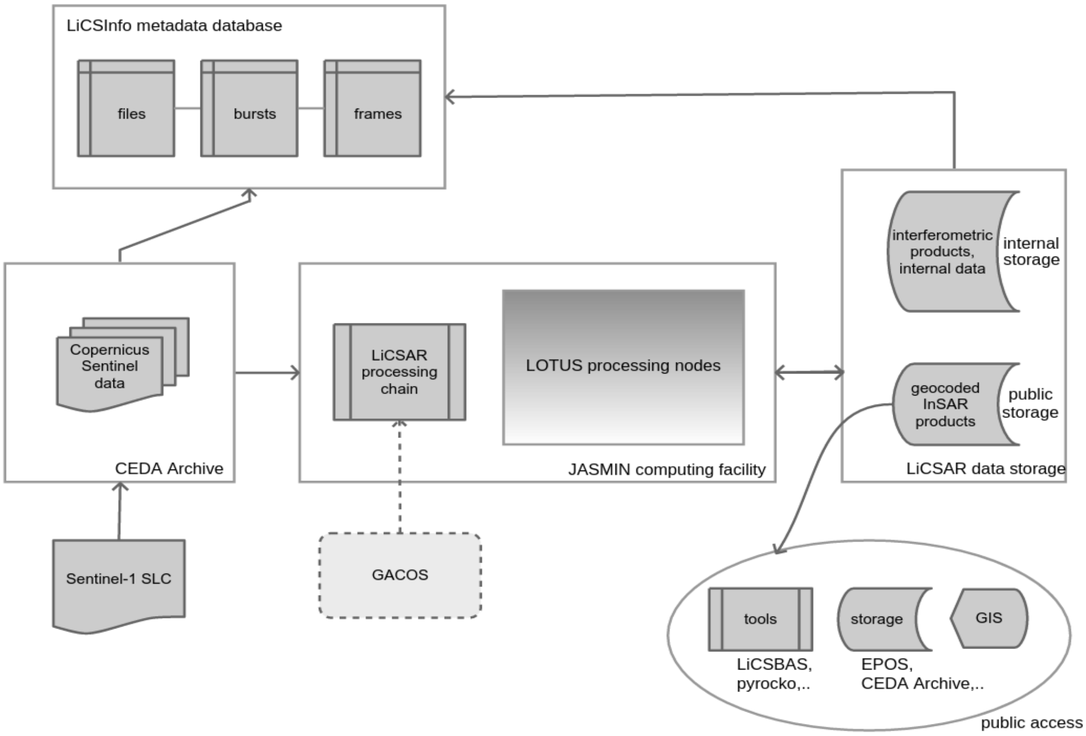

Figure 1. General overview of LiCSAR system architecture: interconnections between storage and computing structures leading the path from Sentinel-1 SLC acquisition to publicly accessible geocoded interferometric products.

2.1 LiCSAR Processing Chain

The aim of the LiCSAR processing chain is to generate interferometric products (see Subsection 4.1.1). The processing workflow to generate interferometric products by LiCSAR is outlined graphically in Fig. 2. Prior to this workflow, each frame should is first defined and initialised within the LiCSInfo database. While frame definition means a logical linking of burst definitions within a frame unit, the initialisation of the frame means a status of having generated base frame data, including the primary epoch SLC and its multilooked intensity raster (MLI), height values based on a digital elevation model (DEM), and other frame-related derived products, such as the three components of the unit vector in the satellite line-of-sight (LOS) for each pixel (E-N-U files), which define the sensitivity to motion in the East North and Up/vertical directions [47]. We currently use a 1 arc-second void-filled version of the SRTM DEM as the basic DEM to derive the base frame data [48]. Some frames are prepared using other topographic models (e.g. ASTER GDEM, JAXA ALOS World 3D or DLR TanDEM-X WorldDEM). The DEM-based frame data are key for geolocation of the products and for estimation and removal of a topographic phase screen in interferograms.

Peer-reviewed version available at *Remote Sensing* **2020**, *12*; doi:10.3390/rs12152430

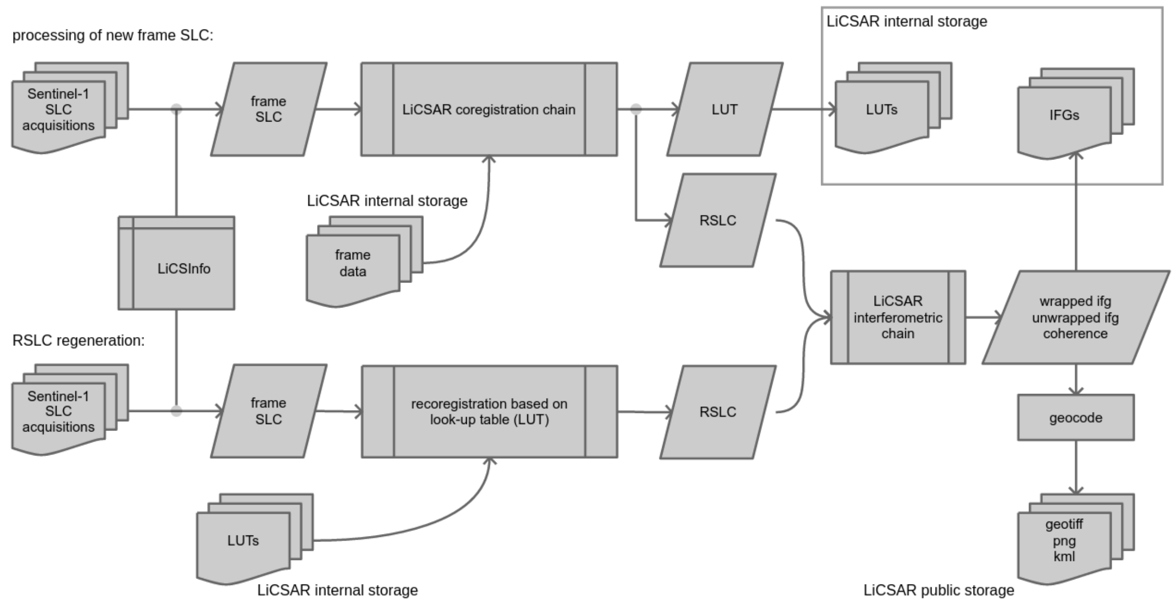

Figure 2. General flowchart of the LiCSAR processing chain

The interferometric processing of Sentinel-1 data for each temporal epoch consists of four steps:

2.1.1. Preparation of frame epoch SLC

In the first step, we identify Sentinel-1 SLC data covering a given temporal epoch (a given date) and containing all or at least some bursts of the given frame definition. Frame burst data are extracted from related files available from some of the source data stores (see Section 2.5) and merged to form a frame epoch SLC. We perform several operations at this stage of processing. Firstly, we apply precise (21 days delay) or restituted orbit ephemerides data generated by the Sentinel-1 Quality Control Subsystem (https://qc.sentinel1.eo.esa.int) and downloaded daily from ASF DAAC. We perform a basic set of checks and corrections, such as padding of missing burst data with zeroes (in case of burst data unavailability for the given epoch), or correction of some known issues, e.g. an azimuth phase shift of -1.25 pixels in the first swath for older data (typically before April 2015) processed by Instrument Processing Facility software version 2.36. Finally, we generate an MLI image using our default parameters, e.g. numbers of looks (4 for direction in azimuth and 20 in range), leading to a pixel spacing of 56x46 m (azimuth x range) in the LOS direction.

2.1.2 Resampling to RSLC

The resampling step is demanding on memory (RAM) and has the longest processing runtime - over 1 hour per epoch using a single processing core. The task of this step is to generate resampled RSLC files and additional supplementary files that can be used later to regenerate RSLC if needed for data reprocessing. The process of generating RSLC and the supplementary files from the epoch SLC is shown in Fig. 3. The following textual description uses estimated processing time (EPT) measured for a typical frame consisting of 39 bursts (13 bursts per swath) and using a single processing core (as experienced at facility described in Section 2.5). The resample procedure (including precise coregistration) follows the approach implemented within the GAMMA command `S1_coreg_TOPS`.

After the first step of generating an epoch SLC (and MLI), a frame DEM (also multilooked by factors of 4x20) is used to provide a DEM-assisted SLC coregistration (GAMMA command `rdc_trans`, EPT ~2 minutes). A preliminary coregistration lookup table (LUT) is generated. In order to increase the precision of SLC coregistration, an intensity cross correlation is performed towards

Peer-reviewed version available at Remote Sensing 2020, 12; doi:10.3390/rs12152430

the frame's primary SLC image (GAMMA command `offset_pwr_tracking`, EPT ~5 minutes) and the estimated offsets are used to update the LUT.

To achieve the high precision coregistration required for TOPS mode interferometry, we use the spectral diversity (SD) technique [49] that estimates a mis-registration offset in azimuth direction, based on inversion of azimuth ramps in interferograms formed from overlaps between bursts of primary and secondary SLC images. To keep a reasonable coherence in the burst overlap interferograms and thus increase reliability of the SD estimate, an existing RSLC is used instead of the primary SLC if its epoch is closer to the epoch being coregistered - this temporally nearest RSLC is recognised as RSLC3. The primary SLC can also serve as RSLC3.

Prior to the SD estimation, a subswath offset estimation (GAMMA command `S1_coreg_subswath_overlap`, EPT 15 minutes) is applied to datasets being processed by an Instrument Processing Facility (IPF) processor differing from the original primary SLC; currently this step is applied only to data from the problematic IPF 2.36.

To estimate the mis-registration using SD, we determine burst overlap regions from the primary SLC metadata (GAMMA command `S1_poly_overlap`). Raster coordinates of the burst overlap regions are used to generate a masked LUT. The masked LUT is applied to resample only the burst overlap regions of the secondary SLC (EPT 20 minutes). The SD azimuth offset is estimated in the burst overlaps between the secondary SLC and RSLC3 applying GAMMA command `S1_coreg_overlap` (to determine the fine coregistration offset within burst overlaps) on the overlap region resampled towards the RSLC3. If the coregistration offset changes by more than 0.0005 pixels, the resample and coregistration of the burst overlaps is repeated up to 5 times (EPT 60+ minutes). Finally, the azimuth pixel offset w.r.t. the LUT is estimated and both are used to resample the original secondary epoch SLC into the RSLC.

After the resampling process, the LiCSAR system stores the LUT and the estimated subpixel shift in azimuth direction (SD estimate) inside an offset refinement file for each RSLC. The data in the LUT can be used later if needed to quickly regenerate an RSLC from SLC data.

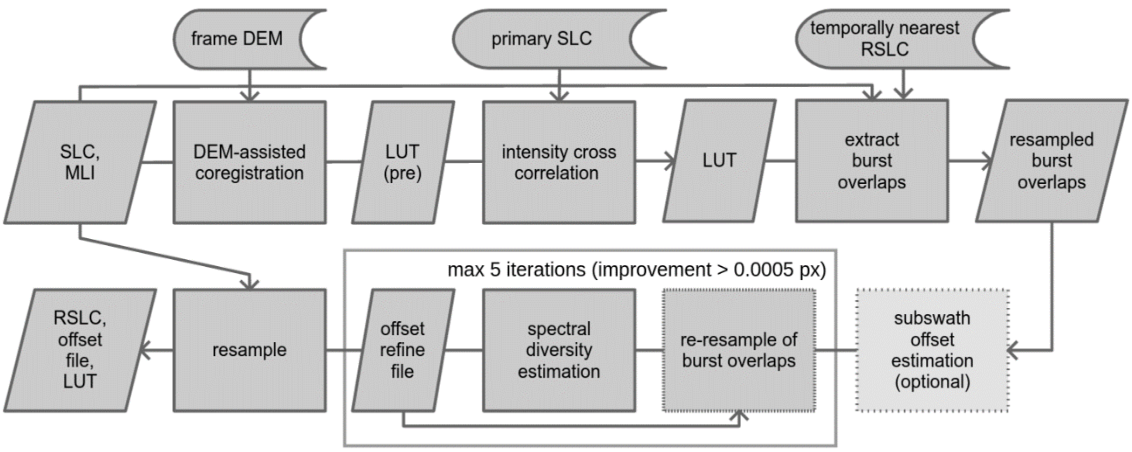

Figure 3. Detailed overview of the coregistration process for a new SLC image (generation of RSLC and complementary files)

2.1.3. Formation of differential interferograms

After ensuring the RSLC mosaics exist for a selected interferometric combination, a simulated DEM-based interferogram is formed containing a prediction of the topographic phase. This topographic phase is removed during the formation of a standard 4x20 multilooked interferogram (GAMMA commands `phase_sim_orb` and `SLC_diff_intf`). By default, interferograms are formed between each epoch and the four preceding and/or following epochs (EPT 15 minutes/interferogram).

2.1.4 Unwrapping interferograms

The interferogram unwrapping is performed using `snaphu` in version 2 [50]. Prior to the unwrapping process, the interferogram is spatially filtered using an adaptive power spectrum filter [51] (GAMMA command `adf` with the parameters *FFT window size* = 32 and *alpha* = 1.0). Points with interferometric coherence lower than 0.5 after filtering are removed prior to unwrapping. A map of statistical costs is generated based on a custom approach that searches for phase consistent pixels, avoiding false phase jumps within a threshold distance [52]. The unwrapping process is run on a single core with no tiling (EPT ~15 minutes/interferogram).

2.2 LiCSInfo Metadata Database

The LiCSInfo metadata database has been developed as the core for our autonomous Sentinel-1 processing system. It contains information on the original Sentinel-1 SLC data files, the LiCSAR frame definitions and the links between them through common burst units. It also stores basic information on processed interferometric products (e.g. file paths, perpendicular baseline) and other useful information (e.g. number of unwrapped pixels as a measure of the product quality). The database is also used to maintain frame update triggers if a frame is set as 'active'. The base structure of the database is depicted in Fig. 4.

Sentinel-1 IWS acquisitions in the form of SLC data are originally distributed as a set of focused burst units (or bursts) within three swaths. Burst metadata, including the geographic coordinates of each burst, can be directly read or inherited from Sentinel-1 annotation files provided within the distributed data. We generate custom unique LiCSAR burst identifiers based on the Zero Doppler azimuth time of the first line of the burst relative to the Ascending Node Crossing (ANX) time. The information is ingested to the table `bursts`. In the case of Sentinel-1 SM acquisitions, the whole areal coverage of the image is set as a burst.

Frame definitions are stored in the table `polygs`. The table includes the generated frame identifier (the naming convention is explained in Section 3) and geographic coordinates of frame corners, among other metadata. The geographic coordinates are generated either from the set of bursts comprising the frame in the case of IWS products or they are set to cover a particular area of interest in case of SM frames. The bursts are linked to the related frames through a lookup table `polygs2bursts`. Geodatabase functions are enabled through tables `bursts2geom` and `polygs2geom`, for both bursts and frames.

Having the basic information about ingested SLC files stored in the table `files` and linked to bursts contained within the files through the lookup table `files2bursts`, it is possible to perform SQL queries such as identifying files related to requested epochs within a selected frame. These structures are also linked to a concurrent LiCSInfo batch processing database (LiCSBatch database) that is used within the LiCSAR FrameBatch processing chain (see Section 2.3). Here, temporary fields linking job-relevant files and bursts are stored in interconnected LiCSBatch tables, as shown in the right panel of Fig. 4. Final product information is stored in products metadata tables (`coherence`, `rslc`, `ifg`).

Finally, earthquake responder tables include basic information on earthquakes and related frames that are ingested to processing by the LiCSAR Earthquake Responder (see Section 2.4). These tables keep track of processing stages for generating pre-seismic, co-seismic and post-seismic interferograms.

Peer-reviewed version available at Remote Sensing 2020, 12; doi:10.3390/rs12152430

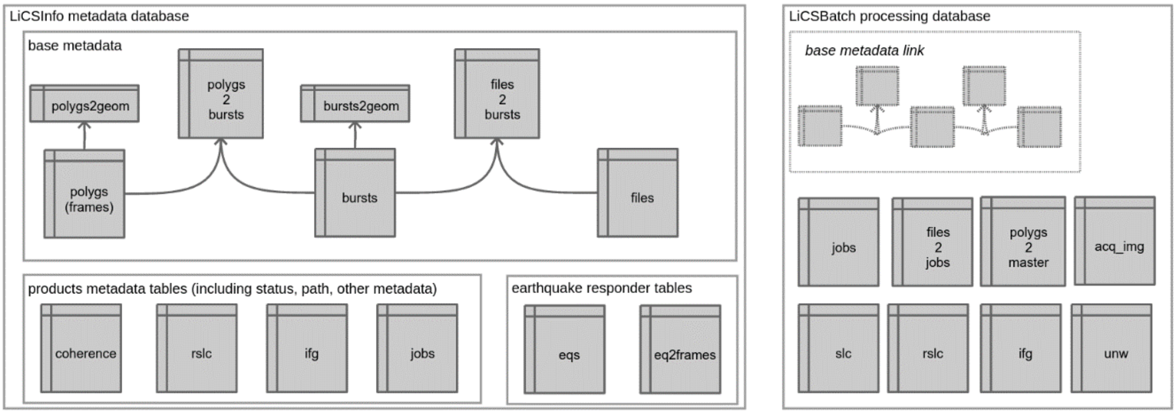

Figure 4. Base structure of LiCSAR databases - LiCSInfo metadata database for storing information on burst and frame definitions, related input files and output products, and earthquake frame data (left) and LiCSinfo batch processing database storing temporary information used for LiCSAR FrameBatch processing chain (right).

2.3 LiCSAR FrameBatch Processing

The LiCSAR FrameBatch package is a set of data structures and algorithms designed to automate frame processing using LiCSAR. It is optimised to run on a computing cluster facility. Our frame processing strategy consists of four parts described below and depicted in Fig. 5. The only required user parameters for starting batch processing for a frame are the frame identifier (frame ID), a toggle for "auto-download" functionality, and, optionally, a start/end date.

2.3.1 Data preparation

At the initial stage, base frame data (pre-processed primary epoch SLC, MLI, DEM-derived frame products etc.) are copied from LiCSAR internal storage to a temporary BatchCache folder. Any products stored in LiCSAR internal storage covering the frame during the requested time period are either linked (interferometric products) or decompressed (7zip-compressed coregistration LUTs or RSLCs). We then use a data-filling script to search for the existence of relevant Sentinel-1 SLC data by querying Copernicus SciHub, comparing the SciHub list to information on the data already ingested to the LiCSInfo metadata database, checking and optionally auto-downloading the relevant SLC data, and then refilling the LiCSInfo database. Optionally, the routine can be set to request the data available at CEDA storage from their Near Line Archive system (NLA, see Section 2.5) automatically though the user is expected to perform such a request prior to the FrameBatch processing (non-autonomous NLA requests are preferred as the complex mechanism of the NLA may induce significant delays in the whole frame processing).

2.3.2 FrameBatch processing chain

After the data preparation step, we generate frame batch processing job definitions. First, epochs covering the requested time period are identified based on LiCSInfo database entries (selecting ingested files that contain bursts related to the frame definition). The epochs are then distributed into processing job definitions for LiCSAR processing steps: SLC generation, coregistration into RSLC, generating interferograms and unwrapping. A maximum of 5 job definitions per step are generated for cases where processing covers the last 3 months (i.e. covering up to 15 epochs, thus distributed into processing of up to 3 epochs per job); a maximum of 20 jobs per step are generated in case of larger requested time scales. A special LiCSBatch database interconnected to LiCSInfo is used - it contains tables allowing us to identify epochs related to each job definition and to keep track of the

Peer-reviewed version available at Remote Sensing 2020, 12; doi:10.3390/rs12152430

progress of jobs. The interferogram generation and unwrapping steps are set to create the standard set of combinations of every epoch with the four preceding epochs.

After the LiCSBatch cache is ready, the processing jobs are started in parallel. Follow-up steps only begin once the preceding steps are finished for given epochs. The processing jobs are optimised to run for less than 24 hours each. Only one processing core is requested per job. Though this approach does not take advantage of increased effectiveness of parallel processing algorithms (e.g. `GAMMA` OpenMPI scripts or `snaphu`), it allows requesting a larger number of parallel jobs in the computing cluster environment.

2.3.3 FrameBatch post-processing

The final stage consists of the following operations: a gap-filling script checks for non-existing wrapped and unwrapped interferograms and runs parallel jobs to generate InSAR products in standard combinations (4 preceding epochs, based on a set of successfully generated RSLCs) and a geocoding script georeferences InSAR products in the GeoTIFF file format and their PNG/KMZ previews (coordinate system WGS-84). An optional routine stores relevant files in the internal LiCSAR storage and the public LiCSAR folder and cleans the temporary processing directory and LiCSBatch cache. We have also developed a state-of-the-art interferogram quality check routine that will be applied before the automatic data store.

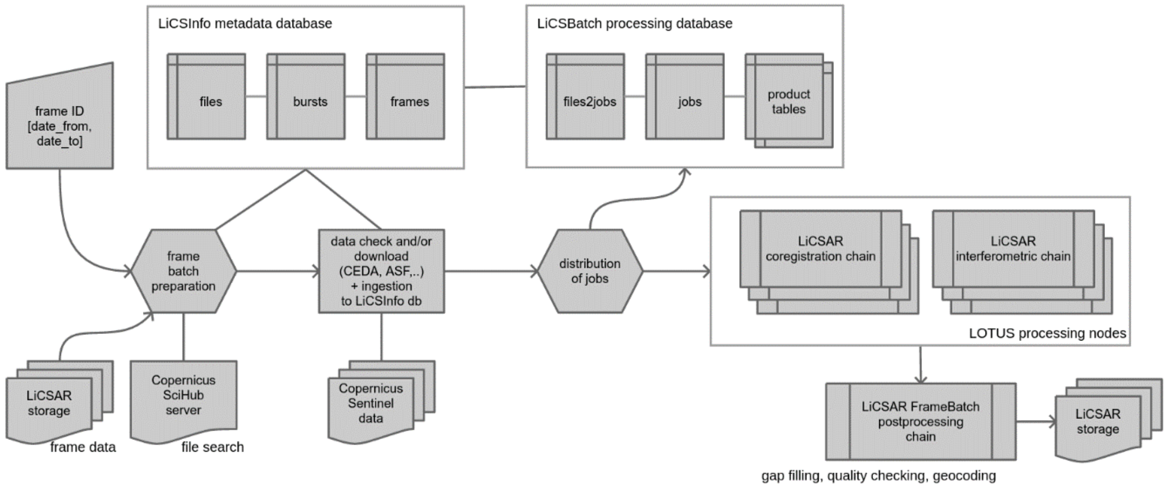

Figure 5. LiCSAR FrameBatch processing chain flowchart – automatic generation of interferometric products for given frame and date limits

2.4 LiCSAR Earthquake Responder

The rapid availability of Sentinel-1 data following acquisition (a few hours), together with the short revisit period for many areas of 6 days, provides a unique opportunity to develop an automatic earthquake response system using the LiCSAR infrastructure. The main objective of this responder is to form co-seismic interferometric pairs in a rapid manner, as well as pre- and post- seismic interferograms, and to make these data widely and freely available to the community. We anticipate that these products have applications for the scientific understanding of events as well as for operational crisis management and disaster mitigation.

Peer-reviewed version available at *Remote Sensing* **2020**, *12*; doi:10.3390/rs12152430

The automatic Earthquake Responder (EQR) within the LiCSAR system works as follows (Fig. 6): a list of current earthquake events with a minimum magnitude of M_w 5.5 is requested through a `libcomcat` python library [53] providing access to the USGS ANSS Comprehensive Earthquake Catalog (ComCat). We then generate a look-up table to estimate the potential radius of the region in which surface deformation caused by the earthquake may have occurred, given the estimated seismological magnitude and 3D location of its hypocentre, accounting for uncertainties in the seismological estimates (see Table 1). This surface radius is used to select all overlapping frames, using the frame definitions from the LiCSInfo database. In the case a selected frame has not been previously initialised, an automatic initialisation is attempted. We then update the EQR-related tables in LiCSInfo database and process at least the last month of data associated with the selected frames using standard LiCSAR parameters and the LiCSAR FrameBatch approach.

We have developed routines for the early identification and fast download of the first post-earthquake Sentinel-1 data and we have created an automatic download routine that uses the Copernicus SciHub service as an alternative data source in order to ensure the availability of the latest data for processing – Sentinel-1 SLC data typically arrive at Copernicus SciHub within a few hours post acquisition, which is earlier than they appear in other accessible data mirrors.

As we use image cross-correlation algorithms within the LiCSAR coregistration step (see Fig. 3), the RSLCs can be generated successfully even without the use of precise orbital ephemerides. Instead, restituted ephemerides (existing already at the time of appearance of the source Sentinel-1 data) are downloaded and applied automatically. We also export co-seismic interferograms as KMZ files (Google Earth data format), in addition to standard InSAR outputs. We link the co-seismic interferogram products to our web based LiCSAR Earthquake Responder map and prepare structures for their automatic ingestion to other community systems (see Section 3). We also aim towards integration of GACOS atmospheric phase screen correction estimates to the final interferograms, noting that GACOS data should be available with a 24 hour delay.

From the perspective of the system architecture, we have arranged a stable sequential procedure that generates coseismic interferograms within 24 hours after the post-event SAR data acquisition. This has been lately substituted by a solution that should allow us to reach co-seismic interferograms within 1-3 hours after the appearance of post-event Sentinel-1 SLC data on the Copernicus SciHub web service. The major difference is specific integration of a dedicated computing node at a distant computing facility for resampling the post-event data with the use of parallel processing and rapid generation of interferometric products.

The frames remain in their active status for a pre-defined period to allow for rapid production of post-seismic interferograms (a post-seismic InSAR response). We scale this time period depending on the magnitude of the event and the number of expected Sentinel-1 images in that location, see Table 1. We also plan to extend the system to volcanic activity rapid response.

Preprints (www.preprints.org) | NOT PEER-REVIEWED | Posted: 3 June 2020

Peer-reviewed version available at Remote Sensing 2020, 12; doi:10.3390/rs12152430

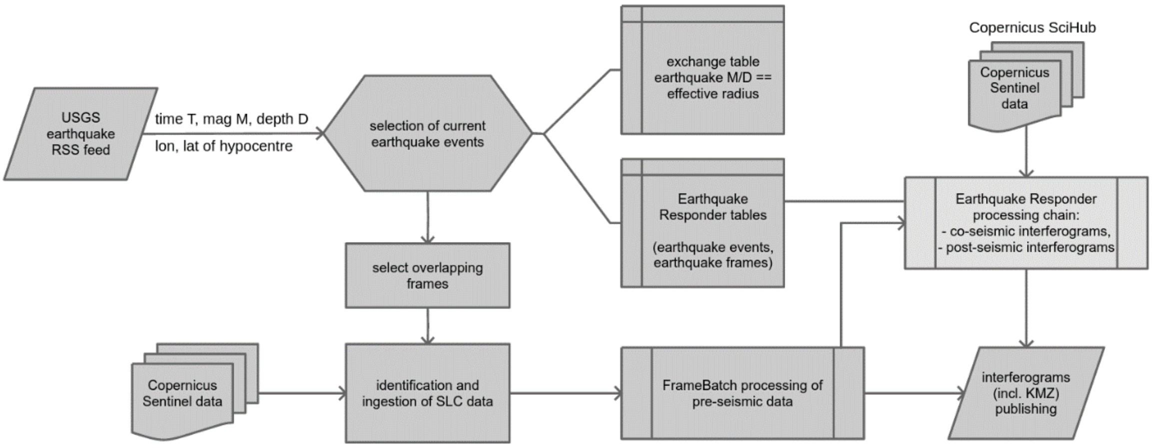

Figure 6. LiCSAR Earthquake Responder processing flowchart. The system leads to the generation of co-seismic and post-seismic interferograms initiated by ingesting information about current earthquakes from the USGS ComCat service.

Table 1. Earthquake response input parameters

Magnitude [M_w]	**Max. depth of hypocentre** [km]	**Surface effect radius from epicentre** [km]	**Postseismic InSAR** [days after earthquake event]
5.5 -5.9	10 – 16	20 – 30	18 – 36
6.0 - 6.9	18 – 63	36 - 167	30 – 84
7.0 - 7.9	73 – 250	199 - 938	54 – 132
8.0 -8.5+	250	1115 - 2500	108 – 156

2.5 Processing and Storage Facility

The LiCSAR processing and storage system runs on CEDA's data analysis infrastructure JASMIN [54]. JASMIN is a computing facility designed for environmental data analysis supercomputing. The processing is carried out mainly using a Load Sharing Facility (LSF) for distributed computer clusters named LOTUS. Since September 2018, JASMIN offers over 40 PB of storage and over 10,000 computing cores distributed between the LOTUS computing cluster and a community cloud [54,55]. LOTUS is managed through IBM's batch queuing system which allows splitting of large processing jobs to run on a requested number of computing cores reserved from LOTUS computing nodes. As we use a dedicated processing queue with a limit of a maximum number of 128 reserved computing cores, we do not use parallel processing algorithms but rather send larger number of processing jobs by reserving one computing core per job.

A community cloud service at CEDA offers managed cloud instances, which we use to run a MySQL/MariaDB database system dedicated to the LiCSInfo database.

Apart from a 350 TB disk area for permanent internal, publicly shared and temporary LiCSAR output files, the JASMIN infrastructure offers direct access to a CEDA Sentinel Mirror Archive (SMA),

Peer-reviewed version available at Remote Sensing 2020, 12; doi:10.3390/rs12152430

a service mirroring data from the Copernicus Sentinel programme [56]. Currently, SMA contains more than 2 PB of data or ~1.6 million individual Copernicus Sentinel data products, over 60% of which is Sentinel-1 SLC data [54]. To cater to the increasing amount of Sentinel data, CEDA has developed the Near Line Archive (NLA) system. The NLA is used to archive older data onto a modern tape storage system. This brings about the limitation of having only the newest data (acquisitions younger than 3 months) available on disk via instant access. Archived data can still be requested - it should take no longer than 24 hours to retrieve data from the NLA into its original location in the SMA directory structure. The restored data can be accessed for a limited period of time (typically 3 weeks). Therefore, the Sentinel-1 data does not have to be downloaded before processing, greatly reducing the time necessary to obtain results.

In cases where the requested Sentinel-1 data are not available at SMA, we use one of the optimised high speed transfer servers at the CEDA JASMIN facility to download the required data from either NASA's ASF DAAC or the Copernicus SciHub server. The necessary SLC datasets are normally available on Copernicus SciHub within a few hours of the satellite acquisition.

Finally, we have established a dedicated computing node at University of Leeds supercomputer (ARC4, http://arc.leeds.ac.uk) that serves as a stable extension of the LiCSAR system, primarily running at CEDA environment. We use the node for running the LiCSAR Earthquake Responder.

3. LiCSAR Products: current state and future trend

The basic InSAR products generated by LiCSAR are original and spatially-filtered wrapped, as well as unwrapped, interferograms and original coherence maps, MLI images for each epoch, and complementary specialised frame images, including incidence angle map files needed for motion vector extraction [47], height values from the DEM used in processing, preprocessed GACOS products, and metadata information (e.g. perpendicular baseline list, date and acquisition time of the primary epoch image). Provided products are georeferenced to the WGS-84 geographic coordinate system. After the processing, results are shared in the form of georeferenced TIFF (GeoTIFF) files and preview bitmap rasters (in PNG format, downsampled to 30% of the original GeoTIFF's dimensions). Some products of special interest (e.g. co-seismic interferograms) are converted into Google Earth KMZ files. In Section 3.1 we elaborate on the contents and coverage of the products.

The LiCSAR products are publicly available through the COMET LiCS products web portal (currently at https://comet.nerc.ac.uk/COMET-LiCS-portal) in the structure described in Section 3.2. Selected InSAR products are or will be available within the European Plate Observing System (EPOS) (http://www.ics-c.epos-eu.org), and the CEDA Archive (https://catalogue.ceda.ac.uk), as well as other platforms (e.g. Google Earth Engine).

3.1 Contents, coverage and update strategy of LiCSAR frame products

LiCSAR systematically uses Sentinel-1 IWS SLC data to generate large-scale multilooked interferograms, georeferenced to the ground resolution of a pixel size of of 10^{-3}x10^{-3} degrees in WGS-84 geographic coordinate system (corresponding to ~100x100 m at the equator). Sentinel-1 datasets are processed, organised and catalogued in frame units. Default frames consist of 39 bursts (13 bursts within each of three observation swaths) – such a standard frame covers an area of around 220x250 km. Our standard frame definitions include overlap of one burst per swath with each neighbouring frame along the orbital track. This enables us to seamlessly merge interferometric outputs from the frames.

Peer-reviewed version available at Remote Sensing 2020, 12; doi:10.3390/rs12152430

We have defined frames globally, but only carry out systematic LiCSAR InSAR analysis on a selection of frames within our current priority areas. The tectonic priorities are the Alpine-Himalayan Belt (572 frames) and East African Rift System (Fig. 7). These frames are currently in the process of being systematic backfilled to a monthly 'rolling' status, in which data will be no more than 1 month out of date. This default status allows us to use the precise orbit ephemerides, which are available 21 days after each acquisition. Frames of a special interest can be switched to a weekly 'rolling' status with interferograms generated using the latest available data (using restituted orbit ephemerides).

The LiCSAR system is also producing Sentinel-1 frame interferograms globally over 80% of the 1331 on-land volcanoes considered active during the Holocene [57]. Frames covering areas with volcanic activity are being updated three times per week and the list of these frames is updated based on new and ongoing volcanic activities reported by the Smithsonian Institution [57]. Figure 7 shows the global distribution of the active volcanoes and the number of interferograms for each of them. We develop routines to augment these frames into a 'live' status, i.e. to have interferograms generated as soon as a new acquisition appears at some of our source data stores.

Interferograms related to recent seismic events are generated by the LiCSAR Earthquake Responder processes. Figure 7 includes locations of earthquakes where LiCSAR generated co-seismic frame interferograms. We are currently testing an updated version of the Earthquake Responder that runs through earthquake-related update routines every 30 minutes. The frequent updates of the processing status of the frames ensure their temporary 'live' status until a specified time after the earthquake (in order to also generate several post-seismic interferograms).

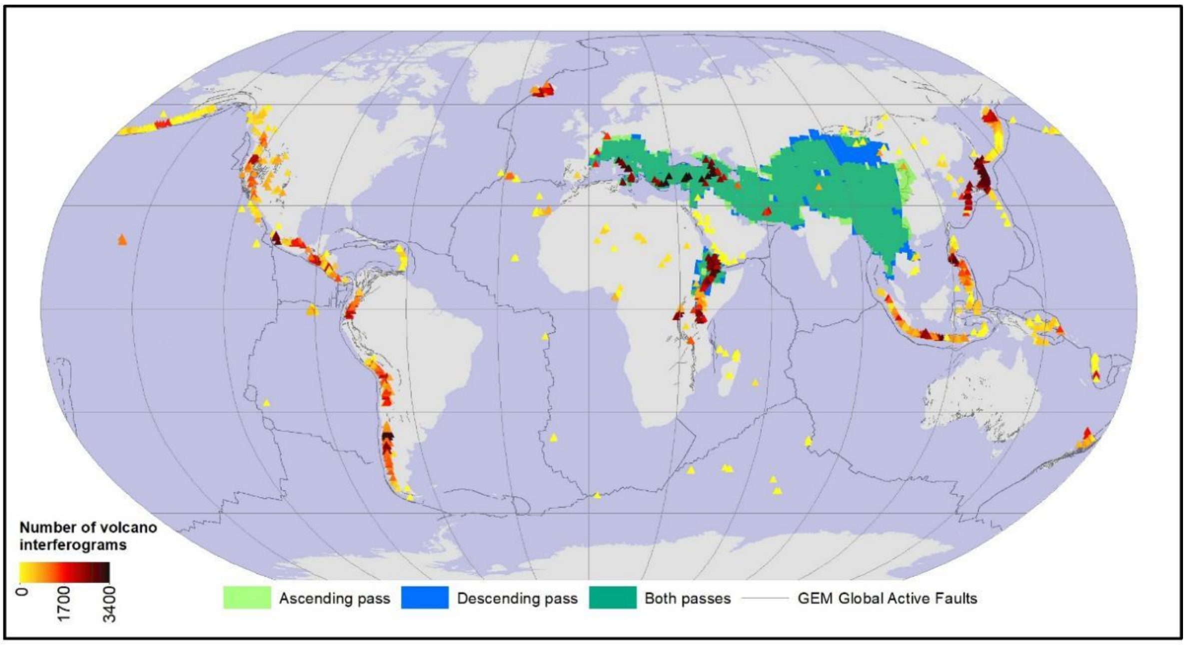

Figure 7. LiCSAR tectonic priority frames (ascending and descending) over the Alpine-Himalayan Belt and the number of interferograms processed by LiCSAR over active volcanoes as of April 2020. Global Active Faults data are from [58].

Due to ESA's acquisition strategy for Sentinel-1, some of the data collected over certain small islands is acquired in stripmap (SM) mode. SM acquisitions are obtained in one of six possible beams. These beams cover a range of incidence angles of approx. 22 - 44° and acquire data in a finer pixel spacing of 1.5-3.1 x 3.6-4.2 (slant range x azimuth) [59]. LiCSAR automated processing produces interferograms for these regions, multi-looked to ~30x30 m resolution, and the same output files and metadata as are generated for IWS acquisition mode products. We have added an automatic

Peer-reviewed version available at Remote Sensing 2020, 12; doi:10.3390/rs12152430

processing functionality for SM acquisitions to incorporate the following volcanic islands to the LiCSAR product database: La Réunion (French territory, Indian Ocean), Fogo (Cabo Verde), Tristan da Cunha (British Overseas Territory, south Atlantic Ocean) and Marion Island (South Africa, sub-antarctic Indian Ocean). To keep SM frames consistent with the LiCSAR system architecture originally designed for IWS data only, we use the geographic area of the SM image as a "burst" in the LiCSInfo database and a subset definition (geographic coordinates of corners covering area of observed island) as a "frame".

One of the major limiting factors of the use of the InSAR in most of tectonic and volcanic applications is the spatiotemporal variability of tropospheric properties. This is of importance especially in cases where deformation and topography are correlated [60]. To address this limitation, we have developed tools for including products for an atmospheric correction, based on the COMET GACOS system developed at the University of Newcastle [46]. GACOS uses an iterative tropospheric decomposition interpolation model that decouples the elevation and turbulent tropospheric delay components estimated from high-resolution ECMWF and GPS data. GACOS corrections are computed for each LiCSAR frame with the same image sizes to facilitate direct use.

3.2 LiCSAR Products File Structure

Figure 8 shows the LiCSAR system file structure hierarchy and naming convention. The blue parts represent the current state and the gray areas show the capabilities which will be available in the future. Starting from the top level, the LiCSAR products are categorised into `175` folders that correspond to the 175 orbital tracks per orbital cycle (relative orbits) of the Sentinel-1 satellites. Currently, a special folder `EQ` contains geocoded outputs of the LiCSAR Earthquake Responder categorised according to the USGS ComCat code for each earthquake.

The naming convention of frame identifiers (used also as folder names for frame related data) has a structure: `OOOP_AAAAA_BBBBBB`, where `OOO` denotes the number of the relative orbit, `P` identifies orbital pass – either descending (D) or ascending (A), `AAAAA` is a colatitude identifier, *i.e.* a complementary angle of the latitude of the frame centre (multiplied by 100), and `BBBBBB` identifies the number of included bursts (three pairs of digits corresponding to number of bursts in each of three Sentinel-1 IWS swaths).

Inside the frame directory, the generated InSAR products are located in the `interferograms` subfolder. The name of each interferometric pair shows the date of acquisition epochs used for that pair. The basic interferometric products reside in each interferometric pair folder as:

- yyyymmdd_yyyymmdd.geo.cc.tif: coherence image (GeoTiFF) of the interferometric pair. The values vary between 1-255 where 1 refers to the lowest coherence values and 255 indicates the highest values of coherence. It is in `uint8` format with 0 as the 'no data' value,

- yyyymmdd_yyyymmdd.geo.cc.png: a gray-scale raster preview of the coherence image (white = maximal coherence). The preview is resized to 30% of the original GeoTIFF,

- yyyymmdd_yyyymmdd.geo.diff_pha.tif: wrapped-phase spatially filtered differential interferogram image (GeoTiFF). The values vary within the range of $-\pi$ to π radians. The phase values pertain to the the satellite LOS, thus the signal can be interpreted as motion away from the satellite if the observed phase difference is positive. The phase values are saved in the file in a `float32` precision with 0 as 'no data' value,

- yyyymmdd_yyyymmdd.geo.diff_unfiltered_pha.tif: wrapped-phase interferogram image (GeoTiFF). The only difference between this and the previous image is that the phases are not spatially filtered.

Peer-reviewed version available at Remote Sensing 2020, 12; doi:10.3390/rs12152430

- yyyymmdd_yyyymmdd.geo.diff.png: a raster preview of the wrapped-phase interferogram (a colour fringe in the direction blue-green-yellow-orange-purple-blue would mean a change of 2π radians towards the satellite). The preview is resized to 30% of the original GeoTIFF,

- yyyymmdd_yyyymmdd.geo.unw.tif: unwrapped phase image in radians (GeoTiFF). Keeping the same rule as the wrapped phase images, the values are in the satellite LOS direction, i.e. positive values mean a range increase (i.e. motion away from from the satellite), while negative values mean a range decrease (*i.e.* motion towards the satellite) perhaps caused by uplift. The format of the file is `float32` with zero values as 'no data' often related to pixels which are masked due to low coherence.

- yyyymmdd_yyyymmdd.geo.unw.png: a raster preview of the unwrapped interferogram, representing interferometric phase values after rewrapping to a scale of 6π per colour cycle (using the same convention for LOS direction as for the wrapped-phase interferogram preview). The image is resized to 30% of the original GeoTIFF,

- yyyymmdd_yyyymmdd.kmz: an optional Google Earth KMZ output is typically generated from full resolution (0.001°) raster previews of the generated interferogram products.

In addition to the interferograms, georeferenced MLI images for each processed epoch are stored in the `epochs` folder in directories corresponding to the acquisition date in the format `yyyymmdd`. The intensity images are produced by space-domain averaging of the SLC images with 4 and 20 as the number of azimuth and range looks respectively. MLI images are generated without a radiometric calibration and only for a co-polarised channel (VV).

Additional files are stored in the `metadata` folder:

- `OOOP_AAAAA_BBBBBB.geo.{E,N,U}.tif`: these files (GeoTiFFs)contain the east (E), north (N) and upward (U) components of the LOS unit vector for each pixel. They are calculated from the SAR look-vector elevation and orientation angle of each pixel, based on the SAR imaging and DEM geometries with the local topography taken into account. The unit vector information can be used, for example, to project E-N-U modeling results or 3-D geodetic observations like GNSS data onto the LOS vector in order to be able to compare them to the LiCSAR results [43],

- `OOOP_AAAAA_BBBBBB.geo.hgt.tif`: this image (GeoTiFF) contains the height values extracted from the DEM used in processing,

- `baselines`: a text file containing the temporal and spatial baselines of each acquisition with respect to the master image,

- `metadata.txt`: a text file containing various other information related to the frame (e.g. primary epoch and acquisition time for its center location, etc.)

Preprints (www.preprints.org) | NOT PEER-REVIEWED | Posted: 3 June 2020
Peer-reviewed version available at Remote Sensing 2020, 12; doi:10.3390/rs12152430

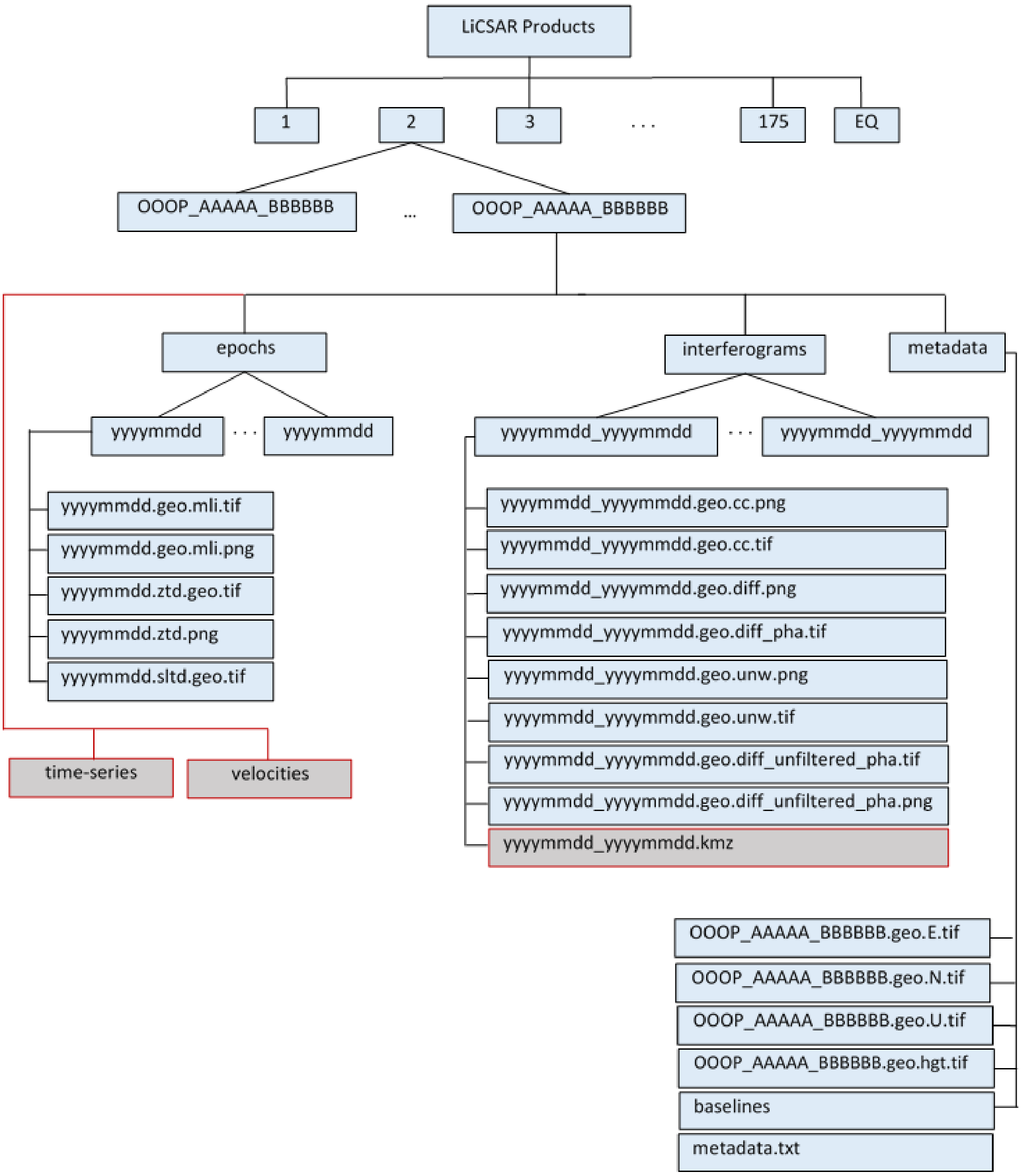

Figure 8. The file structure of the LiCSAR system products publicly available in COMET LiCS portal

In the near future the `time-series` and `velocity` folders will contain outputs stemming from multitemporal InSAR processoring based on the LiCSBAS approach [61]. The main objective of this module (currently still under development) is to generate average displacement velocity maps and time series of displacements for all processed LiCSAR frames. The velocity and time series products will be provided initially in 1 km resolution, with a higher resolution (initially 100 m) over volcanic areas.

GACOS tropospheric delay maps are provided per epoch (in the `epochs` folder) in GeoTIFF format in the same resolution as the other LiCSAR products and in both vertical and LOS direction. The LOS tropospheric delay is stored as a `yyyymmdd.sltd.geo.tif` file. It should allow the user to readily apply the correction to the LiCSAR phase products, for example using the LiCSBAS software [61]. Additionally, we archive the original GACOS tropospheric delay map as

Peer-reviewed version available at *Remote Sensing* **2020**, *12*; doi:10.3390/rs12152430

`yyyymmdd.ztd.geo.tif` and `yyyymmdd.ztd.png` files. Currently only few frames have GACOS products generated during the testing phase.

4. LiCSAR applications for measuring tectonic and volcanic deformations

Since the initial development of the LiCSAR system, numerous research projects have been carried out to study deformation of the Earth's crust using LiCSAR products. Typical deformation sources include magma chambers, dike intrusions, and faults that slip during different phases of the earthquake cycle. Below, we highlight some case studies where LiCSAR has contributed to the monitoring of tectonic activity and volcanic events.

4.1. LiCSAR for Tectonic Applications

Provision of Sentinel-1 InSAR products produced by the LiCSAR processor with a wide spatial coverage increases the potential for large-scale InSAR studies of tectonic processes. Over the past few years, the LiCSAR system has proved to be a powerful tool in various tectonic applications, leading to improved understanding of crustal deformation processes.

The LiCSAR system is currently producing Sentinel-1 interferograms for all the frames covering seisimcally active portions of the Alpine-Himalayan belt (9,000 x 2,000 km), where many of the planet's most deadly earthquakes occur. The LiCSAR Earthquake Responder is actively generating interferometric products for almost every major shallow earthquake affecting continental regions on Earth.

4.1.1. Coseismic interferometric products

As an example, Figure 9 shows three coseismic interferograms from continental earthquakes in different tectonic settings generated in both ascending (left) and descending (right) orbits. They correspond to the July 4, 2019, M_w 7.1 right-lateral strike-slip earthquake in Ridgecrest, California (Fig. 9a), the November 12, 2017, M_w 7.3 dip-slip earthquake in Iran-Iraq border (Fig. 9b), and September 16, 2015, M_w 8.3 dip-slip earthquake in Illapel, Chile (Fig. 9c). Each colour cycle can be interpreted as representing 2.8 centimeters of relative ground displacement in the LOS direction (i.e. towards or away from the satellite). Because the LiCSAR metadata folder includes grids of the unit vector in the satellite LOS at each pixel, the data can easily be used for earthquake source modelling, for example using tools such as Pyrocko [62], which automatically can ingest LiCSAR products.

As an example of other generated InSAR products, Figures 10a and 10b show the unwrapped phase and coherence images corresponding to the Ridgecrest interferogram in Fig. 9b respectively. It should be noted that the phases in Fig. 10a are rewrapped to 6π and therefore the colour cycle here is equal to a 6π phase variation (8.3 cm if it is caused by movement in the LOS). The white areas in the unwrapped image show the areas that were masked based on a coherence threshold to avoid unwrapping errors. These low coherence regions (visible as dark spots in Fig. 10b) can be due to large changes in the ground surface due to surface rupture, ground shaking and high displacement gradients. Fig. 10c is the intensity image of the same frame corresponding to the post-seismic Sentinel-1 image, acquired on August 21, 2019.

Peer-reviewed version available at *Remote Sensing* **2020**, *12*; doi:10.3390/rs12152430

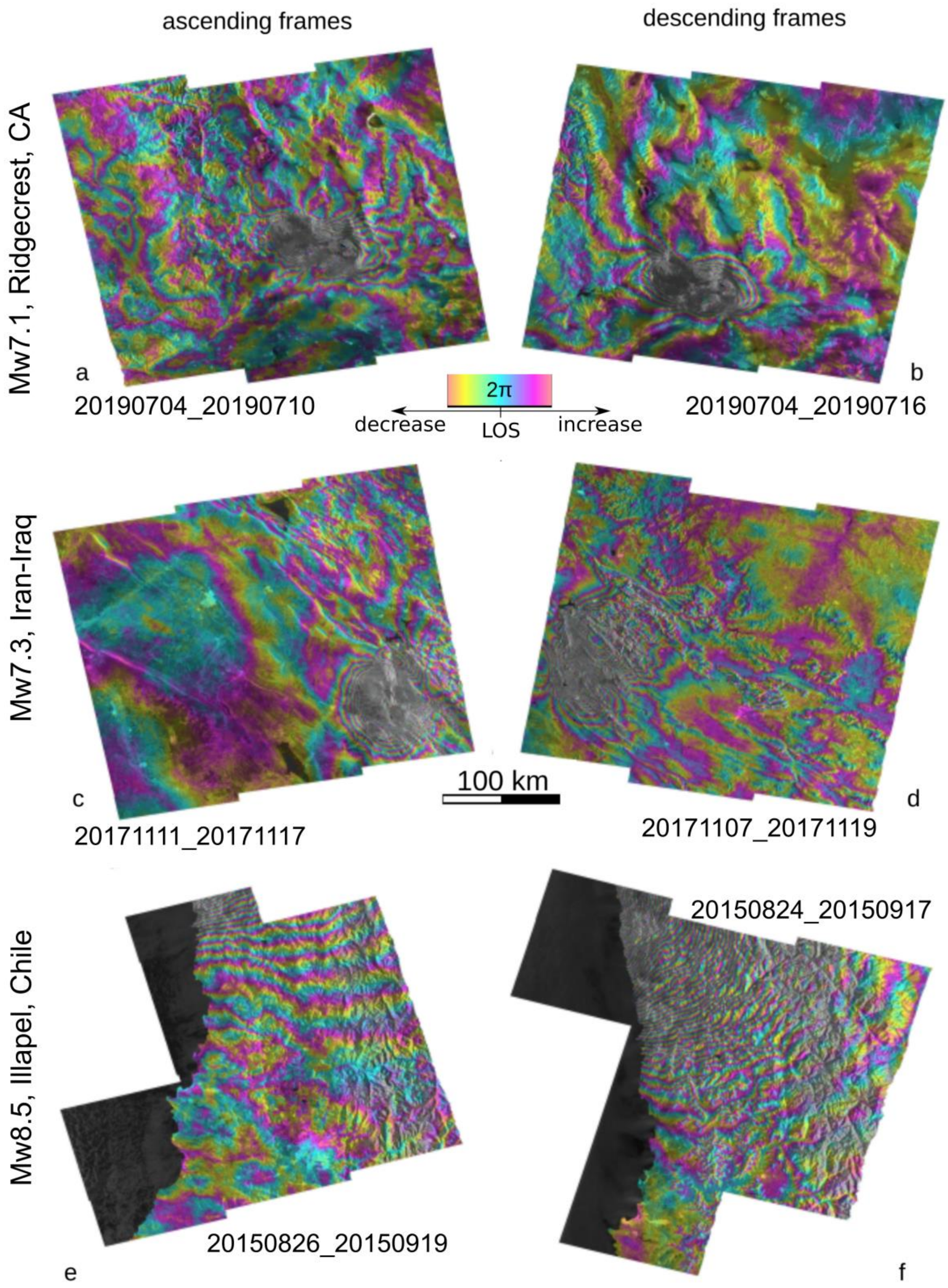

Figure 9. Coseismic interferograms generated in both ascending (left) and descending (right) orbital tracks of Sentinel-1 by the LiCSAR processor for: M_w 7.1 right-lateral, strike-slip earthquake in Ridgecrest, California (July 4, 2019) from (**a**) frame 064A_05410_131313 and (**b**) frame 071D_05377_131313; M_w 7.3 dip-slip earthquake in Iran-Iraq border (November 12, 2017) from (**c**) frame 072A_05489_131313 and (**d**) frame 006D_05509_131313; and M_w 8.3 dip-slip earthquake in Illapel, Chile (September 16, 2015) from (**e**) frame 018A_12301_061311 and (**f**) frame 156D_12184_101305. Note that the deformation from the Illapel earthquake covers too large an area to be completely captured in a single Sentinel-1 frame.

Peer-reviewed version available at Remote Sensing 2020, 12; doi:10.3390/rs12152430

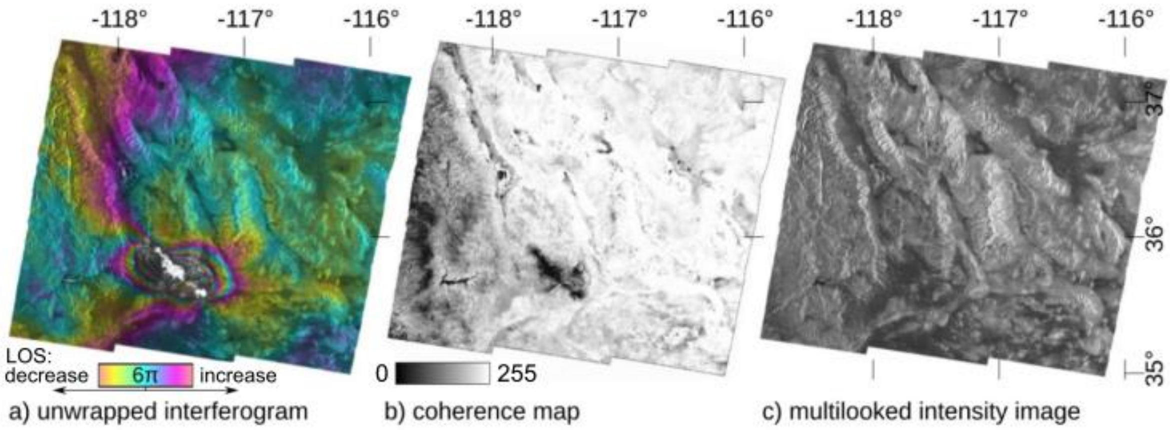

Figure 10. Additional LiCSAR interferometric products over Ridgecrest earthquake (July 4, 2019) of frame 071D_05377_131313 (epochs from 4th and 16th July 2019): (**a**) co-seismic unwrapped phase, (**b**) coherence image and (**c**) radar intensity image from a post-seismic epoch.

4.1.2. Value-added LiCSAR-based products for tectonic studies

An InSAR displacement time series serves as an example of products that can be generated using LiCSAR products. Interferometric products of LiCSAR over Turkey have been used to study the North Anatolian Fault (NAF), a major right-lateral, strike-slip fault accommodating the relative motion between the Anatolian and Eurasian tectonic plates at a rate of ~25 mm/yr [63]. We have processed LiCSAR frames for Anatolia starting with the first Sentinel-1A acquisitions in October 2014 until October 2019 to obtain the average satellite LOS velocities using LiCSBAS [61]. An example of a LOS velocity map for a selected frame, overlain by the main faults, clearly shows the right-lateral interseismic motion across the NAF (Fig. 11a). Figure 11b shows the time-series of cumulative displacement for a sample pixel north of the NAF with respect to a reference pixel located south of the fault. The best-fit LOS velocity of –15.2 mm/year for this pixel is representative of westward movement of the Anatolian microplate. We also see a clear seasonality to the relative LOS motion in this case.

The global coverage of LiCSAR also makes it possible to derive high-resolution, precise and global estimates of tectonic strain rates based on a time series inversion. For example, the LOS velocity for the frame shown in Fig. 11a has been used to derive strain rates for Anatolia [64].

Peer-reviewed version available at Remote Sensing 2020, 12; doi:10.3390/rs12152430

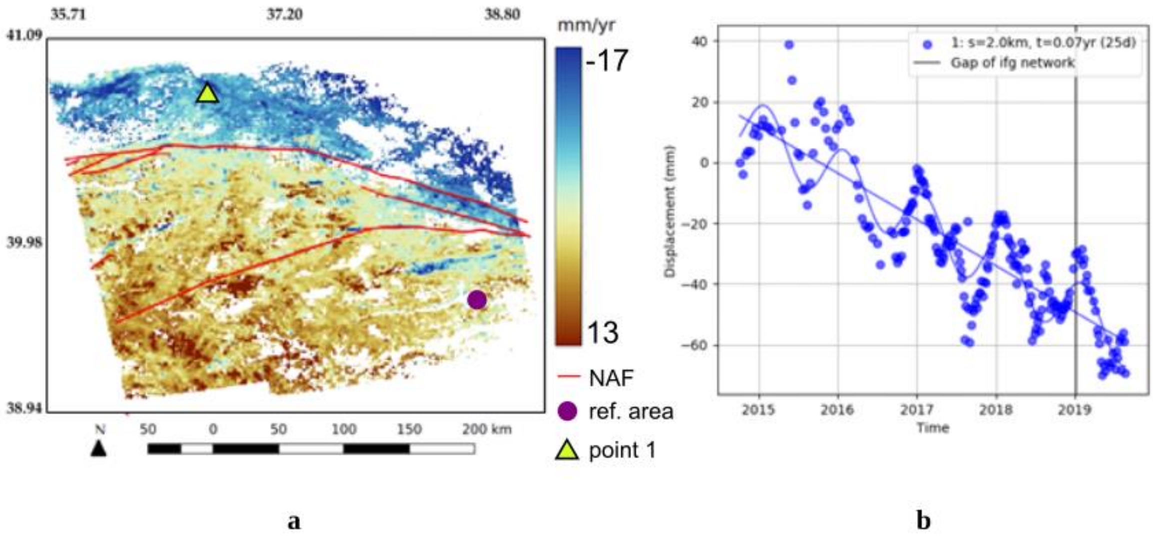

Figure 11. Velocity map generated for an area in the NAF area corresponding to the frame 014A_04939_131313: (**a**) and the displacement time-series (**b**) for a point in the north side of the fault (relative to the reference point on the south) generated using the LiCSAR products and LiCSBAS software. The linear trend and the annual seasonality are also shown by the line and the curve, respectively. The size of the spatial and temporal filters are s = 2 km and t = 25 days.

4.2. LiCSAR for Volcanic Applications

The total number of interferograms calculated for volcanoes is greater than 364,400 (as of May 2020; the number is a count of interferogram subsets around volcanoes). The objectives of volcano processing are to provide a global InSAR dataset to the scientific community and to support the monitoring of ground unrest on any active volcanoes. Because of the large number of products, it becomes impossible to visually check all of them. Therefore, the COMET team has developed several machine learning approaches for automatically detecting ground deformation signals based on blind signal separation methods [25,65] and deep learning techniques [66-68]. The latter algorithms can detect large ground deformation signals in wrapped interferograms, whereas the former approach can detect the onset of slow ground deformation or subtle changes in rate of any background deformation in InSAR time series.

4.2.1. Use of basic interferometric products for volcanic studies

Interferograms of a short temporal baseline in the LiCSAR database can be used to detect strong volcanic deformation related to shallow magma intrusions, such as the March 2017 intrusion at Cerro Azul (Galapagos) and the January 2017 dyke intrusion at Erta Ale (Ethiopia) (Fig 12). The interferogram at Cerro Azul shows two lobes of displacements: ~11 cm of subsidence in the North and ~14 cm of uplift in the South (Fig 12a).

In addition, coherence products can be used to map the emplacement of new volcanic products during an eruption (Fig. 13). The loss of coherence (black) in the central area is an indication of the fresh lava flow emplaced during the 2017 Erta Ale eruption. The production of time series of coherence is useful for tracking flow propagation (e.g. lava initially flows to the NE before flowing to the SW on June 2017) and to derive cumulative flow area [69].

Preprints (www.preprints.org) | NOT PEER-REVIEWED | Posted: 3 June 2020

Peer-reviewed version available at *Remote Sensing* **2020**, *12*; doi:10.3390/rs12152430

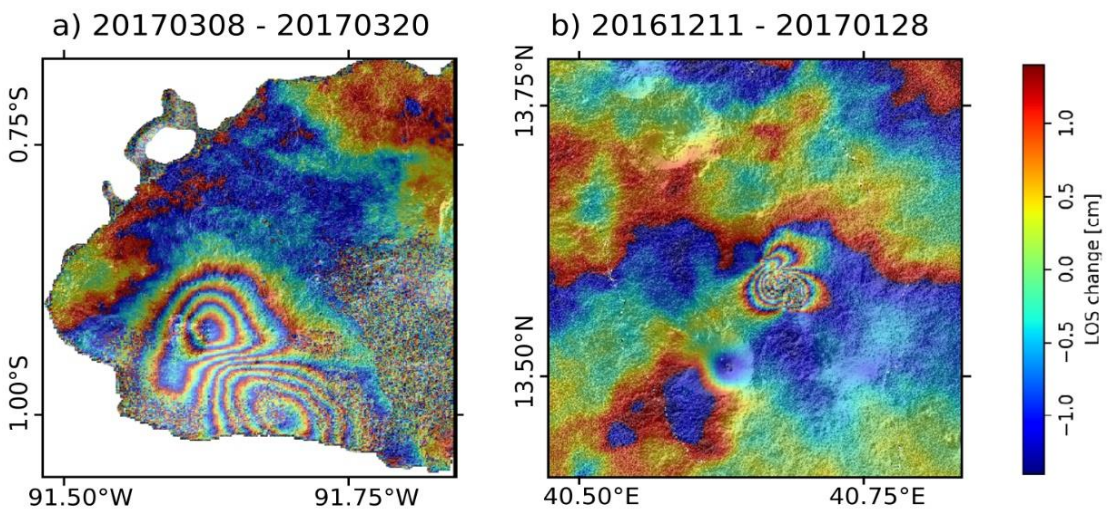

Figure 12. Descending wrapped interferograms generated by the LiCSAR system showing ground deformation associated with (**a**) the March 2017 intrusion at Cerro Azul and (**b**) the January 2017 intrusion at Erta Ale.

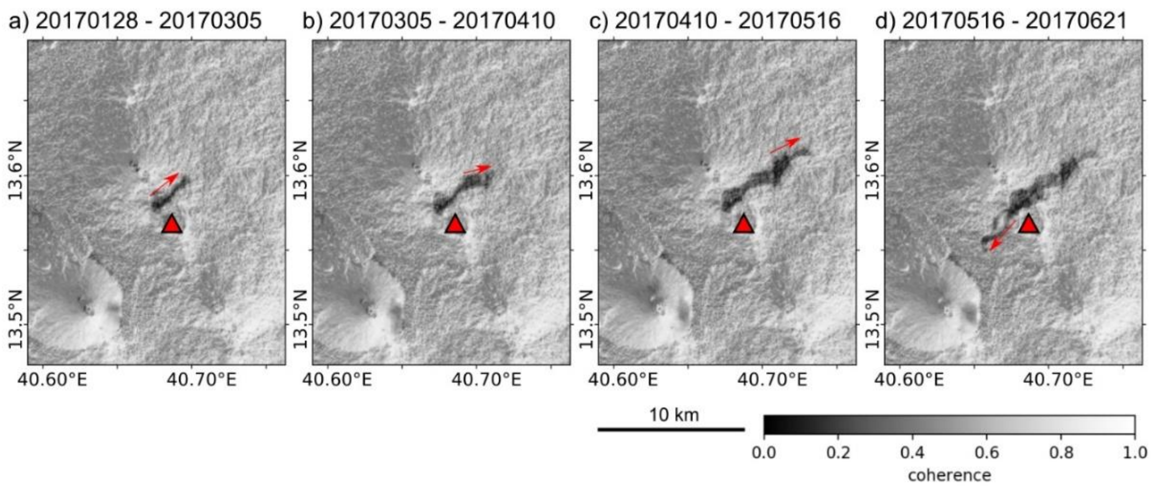

Figure 13. Coherence time series at Erta Ale showing the emplacement of the lava flow during the early stage of the 2017 eruption. The red triangle locates the volcanic edifice and the red arrows indicate the direction of propagation of the lava flow for each period.

4.2.2. Value-added LiCSAR-based products for volcanic studies

LiCSAR unwrapped interferograms can be used to produce time series of ground deformation to track the long-term dynamics of magmatic systems. For example, InSAR time series from the Campi Flegrei caldera (Italy) reveal a persistent uplift signal of about 5.7 cm/yr for the period 2015-2019, consistent with GPS results [61] (Fig. 14). We also observe variations in the associated rates of displacement with period of deceleration (late 2016) and period of acceleration (early 2018).

InSAR time series derived from LiCSAR products have already been successfully used to better understanding the dynamics of magmatic systems during the 2017 eruptions at Mt. Agung (Indonesia) [26] and Erta Ale (Ethiopia) [69].

Peer-reviewed version available at *Remote Sensing* **2020**, *12*; doi:10.3390/rs12152430

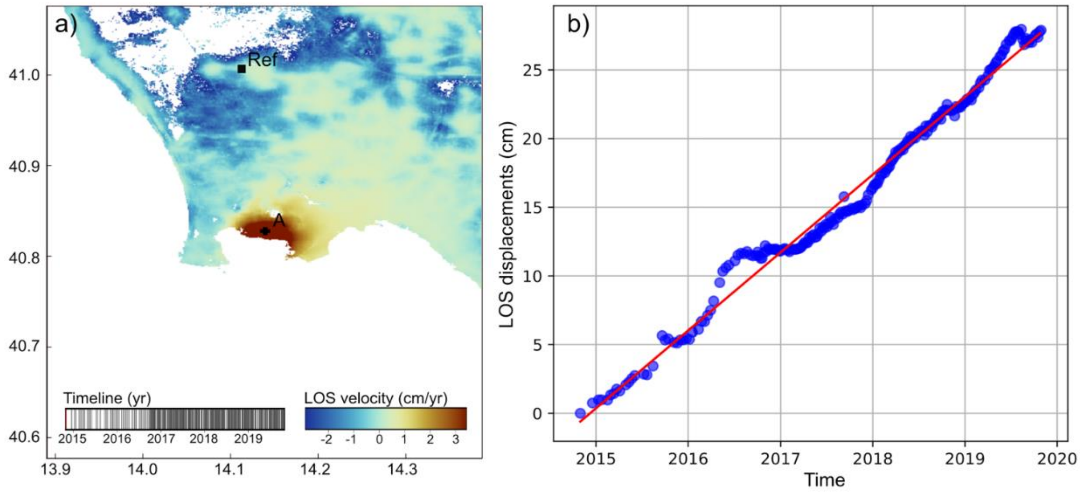

Figure 14. InSAR time series derived from LiCSAR products showing (**a**) the LOS velocity map generated for the Campi Flegrei area (frame ID 022D_04826_121209) and (**b**) the displacement time-series for point A, centered on the caldera, with respect to the reference area located ~20 km north of the caldera.

4.3 LiCSAR for Other Applications

Whilst the focus of this paper is on tectonic and volcanic applications, other uses of LiCSAR data could include hydrosphere, cryosphere, and mass movement studies. For example, temporal decorrelation of glacier surfaces leads to a loss of coherence that can prominently reveal the extent and movement of glaciers [70], which is particularly useful for glaciers covered in debris that are difficult to classify using optical data. LiCSAR coverage across the Alpine-Himalayan belt and in parts of Alaska will facilitate the investigation of glaciers using coherence data. Another potential application of LiCSAR data is to map earthquake-induced landslides. SAR data can be collected through cloud cover, which means data availability is often much quicker than optical acquisitions. Loss of coherence following ground disruption is therefore a potentially useful tool to produce timely regional landslide distribution maps [71].

5. Summary and Conclusions

Here we have introduced the LiCSAR system for observing tectonic and volcanic terrain deformations using Sentinel-1 interferometric processing. The purpose of LiCSAR is to generate and disseminate open interferometric products in formats that are ready for direct use by the research community, particularly in the field of geohazards.

The system aims to continuously monitor actively deforming regions and to provide a response to events such as earthquakes or volcanic eruptions. As of May 2020, the system has processed about 88,000 Sentinel-1 acquisitions and generated more than 270,000 interferograms (around 18 TB). Among the 1,507 LiCSAR frames, 470 frames are related to 1,024 volcanoes. Frames over priority tectonic zones are currently being updated to a 'rolling' status. This is now operational for about 150 frames. Frames covering active volcanoes are processed on a short-term basis (three updates per week), with specific processing structures being developed that should allow generation of interferograms over all active volcanoes as soon as Sentinel-1 SLC data are available (a 'live' status). The 'live' status will also be applied temporarily to frames covering recent earthquakes.

The products are provided for download and visualization in the LiCSAR portal (Fig. 15 or https://comet.nerc.ac.uk/COMET-LiCS-portal).

Peer-reviewed version available at *Remote Sensing* **2020**, *12*; doi:10.3390/rs12152430

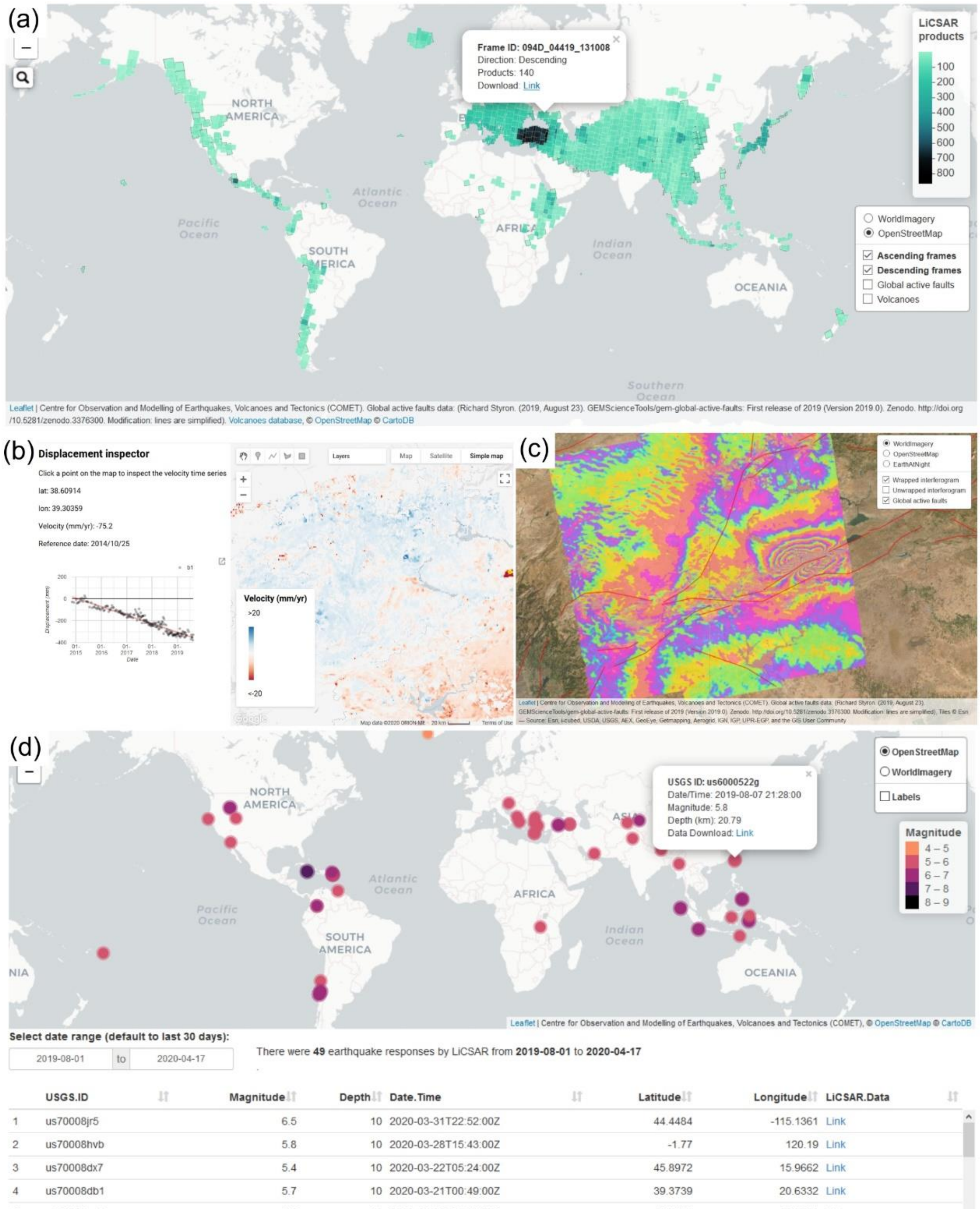

Figure 15. Components of the LiCSAR web portal. (**a**) LiCSAR frame coverage and data download links, (**b**) example of an interactive displacement time series for an area of Turkey (frame ID 116A_05167_121313) derived using LiCSBAS, (**c**) example of an interferogram (of frame ID 116A_05167_121313) processed following the Elazığ earthquake in Turkey (24th January 2020), and (**d**) Earthquake Responder map showing live LiCSAR responses.

Author Contributions: Writing – Original Draft Preparation, M.L. and Y.M.; Software, M.L., P.G., K.S., R.W., E.H., N.G., D.J. and J.R.W.; Investigation, F.A., YuM., J.R.W. and J.E.; Writing – Review & Editing, J.E., E.H., F.A., YuM., P.G., J.R.W., and C.S.W.; Supervision, T.J.W. and A.H.; Funding Acquisition, T.J.W. and A.H.

Funding: This work is supported by The Natural Environment Research Council large grant, "Looking inside the continents from Space" (NE/K010867/1). YuM. is supported by Japan Society for the Promotion of Science Overseas Research Fellowship. J.E. is supported by a Royal Society University Research Fellowship (UF150282). The APC was funded by the University of Leeds. D.J. has received funding from the European Union's Horizon 2020 research and innovation programme under grant agreement No 731070 (EUROVOLC). COMET is the NERC Centre for the Observation and Modelling of Earthquakes, Volcanoes and Tectonics, a partnership between UK Universities and the British Geological Survey.

Acknowledgments: This work used JASMIN, the UK's collaborative data analysis environment (http://jasmin.ac.uk). This paper contains modified Copernicus Sentinel data 2014–2019, processed by ESA, retrieved from NASA ASF DAAC, Copernicus SciHub or CEDA Archive, and analysed by COMET. COMET is the UK Natural Environment Research Council's Centre for the Observation and Modelling of Earthquakes, Volcanoes and Tectonics. Orbital ephemerides by Sentinel-1 Quality Control Subsystem. ASTER GDEM is a product of NASA and METI. Some of the Stripmap and other frames were processed using the ALOS World 3D – 1 arcsec DEM provided by the Japan Aerospace Exploration Agency. This work was partially undertaken on ARC4, part of the High Performance Computing facilities at the University of Leeds, UK.

Conflicts of Interest: The authors declare no conflicts of interest.

References

1. European Space Agency. Copernicus: Sentinel-1. European Space Agency. Available online: Available online: https://directory.eoportal.org/web/eoportal/satellite-missions/c-missions/copernicus-sentinel-1 (accessed on 27 May 2020).
2. Elliott, J.R.; Jolivet, R.; Gonzalez, P.J.; Avouac, J.P.; Hollingsworth, J.; Searle, M.P.; Stevens, V.L. Himalayan megathrust geometry and relation to topography revealed by the Gorkha earthquake. *Nature Geosci* **2016**, *9*, 174-180, doi:10.1038/ngeo2623.
3. Massonnet, D.; Briole, P.; Arnaud, A. Deflation of Mount Etna monitored by spaceborne radar interferometry. *Nature* **1995**, *375*, 567-570, doi:10.1038/375567a0.
4. Peltzer, G.; Rosen, P. Surface Displacement of the 17 May 1993 Eureka Valley, California, Earthquake Observed by SAR Interferometry. *Science* **1995**, *268*, 1333-1336, doi:10.1126/science.268.5215.1333.
5. Atzori, S.; Manunta, M.; Fornaro, G.; Ganas, A.; Salvi, S. Postseismic displacement of the 1999 Athens earthquake retrieved by the Differential Interferometry by Synthetic Aperture Radar time series. *J. Geophys. Res.* **2008**, *113*, doi:10.1029/2007jb005504.
6. Biggs, J.; Burgmann, R.; Freymueller, J.T.; Lu, Z.; Parsons, B.; Ryder, I.; Schmalzle, G.; Wright, T. The postseismic response to the 2002 M 7.9 Denali Fault earthquake: constraints from InSAR 2003–2005. *Geophysical Journal International* **2009**, *176*, 353-367, doi:10.1111/j.1365-246X.2008.03932.x.
7. Gonzalez-Ortega, A.; Fialko, Y.; Sandwell, D.; Alejandro Nava-Pichardo, F.; Fletcher, J.; Gonzalez-Garcia, J.; Lipovsky, B.; Floyd, M.; Funning, G. El Mayor-Cucapah (Mw 7.2) earthquake: Early near-field postseismic deformation from InSAR and GPS observations. *J. Geophys. Res. Solid Earth* **2014**, *119*, 1482-1497, doi:10.1002/2013jb010193.
8. Wang, K.; Fialko, Y. Observations and Modeling of Coseismic and Postseismic Deformation Due To the 2015 Mw 7.8 Gorkha (Nepal) Earthquake. *Journal of Geophysical Research: Solid Earth* **2018**, *123*, 761-779, doi:10.1002/2017jb014620.
9. Walters, R.J.; Holley, R.J.; Parsons, B.; Wright, T.J. Interseismic strain accumulation across the North Anatolian Fault from Envisat InSAR measurements. *Geophys. Res. Lett.* **2011**, *38*, doi:10.1029/2010gl046443.
10. Wright, T.; Parsons, B.; Fielding, E. Measurement of interseismic strain accumulation across the North Anatolian Fault by satellite radar interferometry. *Geophys. Res. Lett.* **2001**, *28*, 2117-2120, doi:10.1029/2000GL012850.
11. Wright, T.J.; Elliott, J.R.; Wang, H.; Ryder, I. Earthquake cycle deformation and the Moho: Implications for the rheology of continental lithosphere. *Tectonophysics* **2013**, *609*, 504-523, doi:10.1016/j.tecto.2013.07.029.

12. Xu, W.; Wu, S.; Materna, K.; Nadeau, R.; Floyd, M.; Funning, G.; Chaussard, E.; Johnson, C.W.; Murray, J.R.; Ding, X., et al. Interseismic Ground Deformation and Fault Slip Rates in the Greater San Francisco Bay Area From Two Decades of Space Geodetic Data. *Journal of Geophysical Research: Solid Earth* **2018**, *123*, 8095-8109, doi:10.1029/2018jb016004.

13. Pritchard, M.E.; Simons, M. An InSAR-based survey of volcanic deformation in the central Andes. *Geochem. Geophys. Geosyst.* **2004**, *5*, doi:10.1029/2003gc000610.

14. Biggs, C.J.; Anthony, E.Y.; Ebinger, C.J. Multiple inflation and deflation events at Kenyan volcanoes, East African Rift. *Geology* **2009**, *37*, 979-982, doi:10.1130/G30133A.1.

15. Biggs, J.; Ebmeier, S.K.; Aspinall, W.P.; Lu, Z.; Pritchard, M.E.; Sparks, R.S.J.; Mather, T.A. Global link between deformation and volcanic eruption quantified by satellite imagery. *Nature Communications* **2014**, *5*, 3471, doi:10.1038/ncomms4471.

16. Juncu, D.; Árnadóttir, T.; Hooper, A.; Gunnarsson, G. Anthropogenic and natural ground deformation in the Hengill geothermal area, Iceland. *J. Geophys. Res. Solid Earth* **2017**, *122*, 692-709, doi:10.1002/2016jb013626.

17. Maghsoudi, Y.; van der Meer, F.; Hecker, C.; Perissin, D.; Saepuloh, A. Using PS-InSAR to detect surface deformation in geothermal areas of West Java in Indonesia. *International Journal of Applied Earth Observation and Geoinformation* **2018**, *64*, 386-396, doi:10.1016/j.jag.2017.04.001.

18. Temtime, T.; Biggs, J.; Lewi, E.; Hamling, I.; Wright, T.; Ayele, A. Spatial and temporal patterns of deformation at the Tendaho geothermal prospect, Ethiopia. *Journal of Volcanology and Geothermal Research* **2018**, *357*, 56-67, doi:10.1016/j.jvolgeores.2018.04.004.

19. Calò, F.; Ardizzone, F.; Castaldo, R.; Lollino, P.; Tizzani, P.; Guzzetti, F.; Lanari, R.; Angeli, M.-G.; Pontoni, F.; Manunta, M. Enhanced landslide investigations through advanced DInSAR techniques: The Ivancich case study, Assisi, Italy. *Remote Sensing of Environment* **2014**, *142*, 69-82, doi:10.1016/j.rse.2013.11.003.

20. Lauknes, T.R.; Piyush Shanker, A.; Dehls, J.F.; Zebker, H.A.; Henderson, I.H.C.; Larsen, Y. Detailed rockslide mapping in northern Norway with small baseline and persistent scatterer interferometric SAR time series methods. *Remote Sensing of Environment* **2010**, *114*, 2097-2109, doi:10.1016/j.rse.2010.04.015.

21. European Space Agency. Sentinel 1 Observation Scenario. Available online: Available online: https://sentinel.esa.int/web/sentinel/missions/sentinel-1/observation-scenario (accessed on 27 May 2020).

22. Elliott, J.R.; Walters, R.J.; Wright, T.J. The role of space-based observation in understanding and responding to active tectonics and earthquakes. *Nature Communications* **2016**, *7*, 13844, doi:10.1038/ncomms13844.

23. Hooper, A.; Wright, T.J.; Spaans, K.; Elliott, J.; Weiss, J.R.; Bagnardi, M.; Hatton, E.L.; Ebmeier, S.K.; Gaddes, M.; Qiu, Q., et al. Global Monitoring of Fault Zones and Volcanoes with Sentinel-1. In Proceedings of IGARSS 2018 - 2018 IEEE International Geoscience and Remote Sensing Symposium, 22-27 July 2018; pp. 1566-1568.

24. Elliott, J. Earth Observation for the assessment of earthquake hazard, risk and disaster management. *Surveys in Geophysics (in review)* **2020**.

25. Gaddes, M.E.; Hooper, A.; Bagnardi, M. Using Machine Learning to Automatically Detect Volcanic Unrest in a Time Series of Interferograms. *Journal of Geophysical Research: Solid Earth* **2019**, *124*, 12304-12322, doi:10.1029/2019jb017519.

26. Albino, F.; Biggs, J.; Syahbana, D.K. Dyke intrusion between neighbouring arc volcanoes responsible for 2017 pre-eruptive seismic swarm at Agung. *Nature Communications* **2019**, *10*, 748, doi:10.1038/s41467-019-08564-9.

27. Zinno, I.; Elefante, S.; Luca, C.D.; Manunta, M.; Lanari, R.; Casu, F. New advances in intensive DInSAR processing through cloud computing environments. In Proceedings of 2015 IEEE International Geoscience and Remote Sensing Symposium (IGARSS), 26-31 July 2015; pp. 5264-5267.

28. Sentinel Application Platform (SNAP). Sentinel-1 Toolbox. Available online: https://step.esa.int/main/toolboxes/sentinel-1-toolbox/ (accessed on 12 Feb 2020).

29. Rosen, P.A.; Gurrola, E.; Sacco, G.F.; Zebker, H. The InSAR scientific computing environment. In Proceedings of EUSAR 2012; 9th European Conference on Synthetic Aperture Radar, 23-26 April 2012; pp. 730-733.

30. Sandwell, D.; Mellors, R.; Tong, X.; Wei, M.; Wessel, P. Open radar interferometry software for mapping surface Deformation. *Eos Trans. AGU* **2011**, *92*, 234-234, doi:10.1029/2011eo280002.

31. Hooper, A.; Zebker, H.; Segall, P.; Kampes, B. A new method for measuring deformation on volcanoes and other natural terrains using InSAR persistent scatterers. *Geophys. Res. Lett.* **2004**, *31*, doi:10.1029/2004gl021737.

32. Werner, C.; Wegmüller, U.; Strozzi, T.; Wiesmann, A. Gamma SAR and interferometric processing software. In Proceedings of Proceedings of the ers-envisat symposium, gothenburg, sweden.

33. GAMMA Remote Sensing (2019). GAMMA Software Information. Available online: https://www.gamma-rs.ch/uploads/media/GAMMA_Software_information_02.pdf (accessed on 12 Feb 2020).

34. Harris-Geospatial (2019). ENVI SARscape - Read, Process, Analyze, and Output Products From SAR Data. Available online: https://www.harrisgeospatial.com/SoftwareTechnology/ENVISARscape.aspx (accessed on 12 Feb 2020).

35. SARPROZ. SARPROZ - the SAR PROcessing Tool by PeriZ. Available online: https://www.sarproz.com/ (accessed on 12 Feb 2020).

36. Lazecky, M.; Hatton, E.; Gonzalez, P. J.; Hlavacova, I.; Jirankova, E.; Dvorak, F.; Sustr, Z.; Martinovic, J. Displacements Monitoring over Czechia by IT4S1 System for Automatized Interferometric Measurements using Sentinel-1 Data, *Remote Sensing* under review.

37. Dong, J.; Metternicht, G.; Hostert, P.; Fensholt, R.; Chowdhury, R.R. Remote sensing and geospatial technologies in support of a normative land system science: status and prospects. *Current Opinion in Environmental Sustainability* **2019**, *38*, 44-52, doi:10.1016/j.cosust.2019.05.003.

38. Sudmanns, M.; Tiede, D.; Lang, S.; Bergstedt, H.; Trost, G.; Augustin, H.; Baraldi, A.; Blaschke, T. Big Earth data: disruptive changes in Earth observation data management and analysis? *International Journal of Digital Earth* **2019**, 10.1080/17538947.2019.1585976, 1-19, doi:10.1080/17538947.2019.1585976.

39. ESA Thematic Exploitation Platform. Available online: https://tep.eo.esa.int/home (accessed on 13 Feb 2020).

40. Geohazard Exploitation Platform (GEP) Available online: https://geohazards-tep.eu/ (accessed on 13 Feb 2020).

41. ESA's Grid Processing On Demand (G-POD) environment. Available online: https://gpod.eo.esa.int/ (accessed on 13 Feb 2020).

42. Galve, J.P.; Pérez-Peña, J.V.; Azañón, J.M.; Closson, D.; Caló, F.; Reyes-Carmona, C.; Jabaloy, A.; Ruano, P.; Mateos, R.M.; Notti, D., et al. Evaluation of the SBAS InSAR Service of the European Space Agency's Geohazard Exploitation Platform (GEP). *Remote Sensing* **2017**, *9*, 1291, doi:10.3390/rs9121291.

43. Bally, P.; Pinto, S. The Geohazards Exploitation Platform (GEP). In Proceedings of FRINGE, Frascati, Italy.

44. Bekaert, D.P.; Karim, M.; Linick, J.P.; Hua, H.; Sangha, S.; Lucas, M.; Malarout, N.; Agram, P.S.; Pan, L.; Owen, S.E. Development of open-access Standardized InSAR Displacement Products by the Advanced Rapid Imaging and Analysis (ARIA) Project for Natural Hazards. In Proceedings of AGU Fall Meeting 2019.

45. Wegmüller, U.; Werner, Ch.; Strozzi, T.; Wiesmann, A.; Frey, O.; Santoro, M. Sentinel-1 Support in the GAMMA Software. *Procedia Computer Science* **2016**, *100*, 1305-1312, doi:10.1016/j.procs.2016.09.246.

46. Yu, C.; Li, Z.; Penna, N.T.; Crippa, P. Generic Atmospheric Correction Model for Interferometric Synthetic Aperture Radar Observations. *Journal of Geophysical Research: Solid Earth* **2018**, *123*, 9202-9222, doi:10.1029/2017jb015305.

47. Wright, T.J.; Parsons, B.E.; Lu, Z. Toward mapping surface deformation in three dimensions using InSAR. *Geophys. Res. Lett.* **2004**, *31*, doi:10.1029/2003gl018827.

48. Farr, T.G.; Rosen, P.A.; Caro, E.; Crippen, R.; Duren, R.; Hensley, S.; Kobrick, M.; Paller, M.; Rodriguez, E.; Roth, L., et al. The Shuttle Radar Topography Mission. *Reviews of Geophysics* **2007**, *45*, doi:10.1029/2005RG000183.

49. Yagüe-Martínez, N.; Prats-Iraola, P.; González, F.R.; Brcic, R.; Shau, R.; Geudtner, D.; Eineder, M.; Bamler, R. Interferometric Processing of Sentinel-1 TOPS Data. *IEEE Transactions on Geoscience and Remote Sensing* **2016**, *54*, 2220-2234, doi:10.1109/TGRS.2015.2497902.

50. Chen, C.W.; Zebker, H.A. Phase unwrapping for large SAR interferograms: statistical segmentation and generalized network models. *IEEE Transactions on Geoscience and Remote Sensing* **2002**, *40*, 1709-1719, doi:10.1109/TGRS.2002.802453.

51. Goldstein, R.M.; Werner, C.L. Radar interferogram filtering for geophysical applications. *Geophysical Research Letters* **1998**, *25*, 4035-4038, doi:doi:10.1029/1998GL900033.

52. Hooper, A. A statistical-cost approach to unwrapping the phase of InSAR time series. In Proceedings of Proceedings of the International Workshop on ERS SAR Interferometry, Frascati, Italy

53. USGS. LIBCOMCAT. Available online: https://github.com/usgs/libcomcat/ (accessed on 27 May 2020).

54. Lawrence, B.N.; Kunkel, J.M.; Churchill, J.; Massey, N.; Kershaw, P.; Pritchard, M. Beating data bottlenecks in weather and climate science. . Available online: https://www.bnlawrence.net/assets/papers/LawEA18.pdf (accessed on 12 Feb 2020).

55. Lawrence, B.N.; Bennett, V.L.; Churchill, J.; Juckes, M.; Kershaw, P.; Pascoe, S.; Pepler, S.; Pritchard, M.; Stephens, A. Storing and manipulating environmental big data with JASMIN. In Proceedings of 2013 IEEE International Conference on Big Data, 6-9 Oct. 2013; pp. 68-75.

56. European Space Agency. Sentinel 1A C-band Synthetic Aperture Radar (SAR): Interferometric Wide (IW) mode Single Look Complex (SLC) Level 1 data. Available online: https://catalogue.ceda.ac.uk/uuid/f7014a8d35b648a5983a681fa346d8fc (accessed on 27 May 2020).

57. Global Volcanism Program. Volcanoes of the World, v. 4.8.5. Venzke, E (ed.). Smithsonian Institution. **2013**, 10.5479/si.GVP.VOTW4-201, doi:10.5479/si.GVP.VOTW4-201.

58. Styron, R. GEMScienceTools/gem-global-active-faults: First release of 2019 (Version 2019.0). *ZENODO* **2019**, http://doi.org/10.5281/zenodo.3376300, doi:http://doi.org/10.5281/zenodo.3376300.

59. European Space Agency. Sentinel-1 strip map mode. Available online: https://sentinel.esa.int/web/sentinel/technical-guides/sentinel-1-sar/products-algorithms/level-1/single-look-complex/stripmap (accessed on 12 Feb 2020).

60. Shen, L.; Hooper, A.; Elliott, J. A Spatially Varying Scaling Method for InSAR Tropospheric Corrections Using a High-Resolution Weather Model. *Journal of Geophysical Research: Solid Earth* **2019**, *124*, 4051-4068, doi:10.1029/2018jb016189.

61. Morishita, Y.; Lazecky, M.; Wright, T.J.; Weiss, J.R.; Elliott, J.R.; Hooper, A. LiCSBAS: An Open-Source InSAR Time Series Analysis Package Integrated with the LiCSAR Automated Sentinel-1 InSAR Processor. *Remote Sensing* **2020**, *12*, 424.

62. Heimann, S.; Vasyura-Bathke, H.; Sudhaus, H.; Isken, M.P.; Kriegerowski, M.; Steinberg, A.; Dahm, T. A Python framework for efficient use of pre-computed Green's functions in seismological and other physical forward and inverse source problems. *Solid Earth* **2019**, *10*, 1921-1935, doi:10.5194/se-10-1921-2019.

63. Hussain, E.; Hooper, A.; Wright, T.J.; Walters, R.J.; Bekaert, D.P.S. Interseismic strain accumulation across the central North Anatolian Fault from iteratively unwrapped InSAR measurements. *J. Geophys. Res. Solid Earth* **2016**, *121*, 9000-9019, doi:10.1002/2016jb013108.

64. Weiss, J.R.; Walters, R.J.; Morishita, Y.; Wright, T.J.; Lazecky, M.; Wang, H.; Hussain, E.; Hooper, A.J.; Elliott, J.R.; Rollins, C., et al. High-resolution surface velocities and strain for Anatolia from Sentinel-1 InSAR and GNSS data, Geophysical Research Letters, [preprint] 2020, DOI: 10.31223/osf.io/8xa7j

EarthArXiv. Preprint submitted to Geophysical Research Letters **2020**, DOI: 10.31223/osf.io/8xa7j doi:DOI: 10.31223/osf.io/8xa7j

65. Gaddes, M.E.; Hooper, A.; Bagnardi, M.; Inman, H.; Albino, F. Blind Signal Separation Methods for InSAR: The Potential to Automatically Detect and Monitor Signals of Volcanic Deformation. *Journal of Geophysical Research: Solid Earth* **2018**, *123*, 10,226-210,251, doi:10.1029/2018jb016210.

66. Anantrasirichai, N.; Biggs, J.; Albino, F.; Bull, D. A deep learning approach to detecting volcano deformation from satellite imagery using synthetic datasets. *Remote Sensing of Environment* **2019**, *230*, 111179, doi:10.1016/j.rse.2019.04.032.

67. Anantrasirichai, N.; Biggs, J.; Albino, F.; Bull, D. The Application of Convolutional Neural Networks to Detect Slow, Sustained Deformation in InSAR Time Series. *Geophysical Research Letters* **2019**, *46*, 11850-11858, doi:10.1029/2019gl084993.

68. Anantrasirichai, N.; Biggs, J.; Albino, F.; Hill, P.; Bull, D. Application of Machine Learning to Classification of Volcanic Deformation in Routinely Generated InSAR Data. *Journal of Geophysical Research: Solid Earth* **2018**, *123*, 6592-6606, doi:10.1029/2018jb015911.

69. Moore, C.; Wright, T.; Hooper, A.; Biggs, J. The 2017 Eruption of Erta 'Ale Volcano, Ethiopia: Insights Into the Shallow Axial Plumbing System of an Incipient Mid-Ocean Ridge. *Geochemistry, Geophysics, Geosystems* **2019**, *20*, 5727-5743, doi:10.1029/2019gc008692.

70. Atwood, D.K.; Meyer, F.; Arendt, A. Using L-band SAR coherence to delineate glacier extent. *Canadian Journal of Remote Sensing* **2010**, *36*, S186-S195, doi:10.5589/m10-014.

71. Burrows, K.; Walters, R.J.; Milledge, D.; Spaans, K.; Densmore, A.L. A New Method for Large-Scale Landslide Classification from Satellite Radar. *Remote Sensing* **2019**, *11*, 237.